

# X-ray evidence for multiphase hot gas with nearly solar Fe abundances in the brightest groups of galaxies

David A. Buote<sup>1,2</sup><sup>1</sup> *UCO/Lick Observatory, University of California at Santa Cruz, Santa Cruz, CA 95064, U.S.A.*<sup>2</sup> *AXAF Fellow*

2 December 2024

## ABSTRACT

We analyze the *ASCA* spectra accumulated within  $\sim 100$  kpc radii of 12 of the brightest groups of galaxies. Upon fitting isothermal models (1T) jointly to the *ASCA* SIS and GIS spectra we obtain fits for most groups that are of poor or at best marginal quality and give very sub-solar metallicities similar to previous studies,  $\langle Z \rangle = 0.29 \pm 0.12 Z_{\odot}$ . Two-temperature models (2T) provide significantly better fits for 11 out of the 12 groups and in every case have metallicities that are substantially larger than obtained for the 1T models,  $\langle Z \rangle = 0.75 \pm 0.24 Z_{\odot}$ . Although not very well constrained, for most of the groups absorption in excess of the Galactic value is indicated for the cooler temperature component of the 2T models. A simple multiphase cooling flow model gives results analogous to the 2T models including large metallicities,  $\langle Z \rangle = 0.65 \pm 0.17 Z_{\odot}$ . The nearly solar Fe abundances and also solar  $\alpha/\text{Fe}$  ratios indicated by the 2T and cooling flow models are consistent with the standard models of chemical enrichment of ellipticals, groups, and clusters.

Thus, we have shown that the very sub-solar Fe abundances and Si/Fe enhancements obtained from previous studies are an artifact of their fitting isothermal models to the X-ray spectra which also has been recently demonstrated for the brightest elliptical galaxies. Owing to the importance of these results for interpreting X-ray spectra, in an appendix we use simulated *ASCA* observations to examine in detail the “Fe bias” and “Si bias” associated with the spectral fitting of ellipticals, groups, and clusters of galaxies.

**Key words:** galaxies: general – galaxies: evolution – X-rays: galaxies.

## 1 INTRODUCTION

The hot gas in elliptical galaxies, groups, and clusters of galaxies is thought to be enriched with metals by material ejected by supernovae. Hence, the abundances in the hot gas record the star formation history of these systems and therefore probe the rates of Type Ia and Type II supernovae as well as the shape of the IMF (for reviews see Renzini 1997, 1999). Since the hot gas in these systems emits at temperatures  $T \sim 10^7\text{--}10^8$  °K ( $\sim 1\text{--}10$  keV), X-ray observations are the preferred means to determine the abundances in the hot gas.

Spatial analyses of the X-ray surface brightness profiles of groups of galaxies using *ROSAT* (Trümper 1983) indicate that the hot gas typically extends out to distances in excess of 100 kpc (e.g. Pildis, Bregman, & Evrard 1995; Davis et al. 1996; Ponman et al. 1996; Trinchieri, Fabbiano, & Kim 1997) and also suggest that the gas is divided into distinct compo-

nents corresponding to the halo of the central galaxy and an extended component for the surrounding group (Mulchaey & Zabludoff 1998; also see Ikebe et al. 1996). These studies typically obtain average temperatures of  $T \sim 1\text{--}2$  keV from analysis of the *ROSAT* PSPC spectra and also find evidence for positive temperature gradients in some groups (Trinchieri et al. 1997; Mulchaey & Zabludoff 1998). Despite the evidence for temperature gradients, the abundances reported by the *ROSAT* studies are obtained from isothermal spectral models from which very sub-solar Fe abundances are inferred (the lone exception being NGC 533 – Trinchieri et al. 1997).

Recent analyses of the *ASCA* data (Tanaka et al. 1994) of groups also indicate rising temperature profiles for some groups (Finoguenov et al. 1999; Finoguenov & Ponman 1999). Yet, similar to the *ROSAT* studies, isothermal models are used to obtain the abundances in the hot gas of these systems again giving very sub-solar Fe abundances and, in

arXiv:astro-ph/9903278v1 18 Mar 1999

some cases, Si/Fe ratios in excess of solar (Fukazawa et al. 1998; Davis, Mulchaey, & Mushotzky 1999; Finoguenov et al. 1999; Finoguenov & Ponman 1999).

The very sub-solar Fe abundances for the hot gas in groups of galaxies deduced by these studies are less than those of galaxy clusters and thus pose a problem for the standard models of chemical enrichment (e.g. Renzini 1997). To reconcile these observations with the standard models it has to be postulated that galaxy groups accrete a significant amount of primordial gas after they have spent most of their evolution expelling gas. The unattractive features of this scenario are discussed by Renzini (1994).

These results for groups are in every way analogous to those initially obtained for ellipticals with *ROSAT* (e.g. Davis & White 1996) and *ASCA* (e.g. Matsumoto et al. 1997). Recently, however, Buote & Fabian (1998, hereafter BF) and Buote (1999, hereafter B99) have demonstrated that models having at least two temperature components in the hot gas are required to explain the *ASCA* spectra of the brightest ellipticals. These multiphase models agree with the positive temperature gradients indicated by the *ROSAT* data unlike the isothermal models (B99).

Perhaps most importantly BF and B99 also showed that the Fe abundances determined from the multiphase spectral models of the brightest ellipticals are consistent with solar in stark contrast to the very sub-solar values obtained from isothermal models. This strong dependence of the Fe abundance on the spectral model indicates that one cannot obtain a reasonable estimate of the Fe abundance by using an isothermal model if the hot gas consists of multiple temperature components. Similar problems also arise when determining the  $\alpha$ /Fe ratios (B99).

Since the spectral properties of the brightest ellipticals are so similar to groups, it should be expected that similar results for the Fe abundance also apply to groups of galaxies. To investigate this issue we selected for analysis the groups from the sample of Davis et al. (1999) having the highest quality *ASCA* data suitable for detailed spectral analysis. In addition, we included the group NGC 1132 since Mulchaey & Zabludoff (1999) argue that it has properties similar to bright groups despite that fact that it has no large galaxies aside from NGC 1132. Our final sample consists of 12 galaxies whose properties are listed in Table 1.

The paper is organized as follows. In section 2 we present the observations and discuss the data reduction. We define the models used for broad-band spectral fitting<sup>\*</sup> in section 3.1.1 and discuss calibration and fitting issues in section 3.1.2. The results for the broad-band spectral fitting analysis are presented in section 3.2. We discuss the implications of our results in section 4 and present our conclusions in section 5. Finally, in Appendix A we use simulated *ASCA* observations to examine in detail the “Fe bias” and “Si bias” associated with the spectral fitting of ellipticals, groups, and clusters of galaxies.

\* We focus on the broad-band spectral analysis since B99 found that individual line ratios of Si and S place only weak constraints on the spectral models of the brightest elliptical galaxies which have data of significantly higher S/N than the groups in our sample.

## 2 ASCA OBSERVATIONS AND DATA REDUCTION

The *ASCA* satellite consists of two X-ray CCD cameras (Solid State Imaging Spectrometers – SIS0 and SIS1) and two proportional counters (Gas Imaging Spectrometers – GIS2 and GIS3) each of which is illuminated by its own X-ray telescope (XRT). The SIS has superior energy resolution and effective area below  $\sim 7$  keV while the GIS has a larger field of view. Although the point spread function (PSF) of each XRT has a relatively sharp core, the wings of the PSF are quite broad (half power diameter  $\sim 3'$ ) and increase markedly for energies above a few keV (e.g. Kunieda et al. 1995). As in our previous studies (e.g. B99) we do not attempt to analyze the spatial distribution of the *ASCA* data of these sources because of the large, asymmetric, energy-dependent PSF. Rather, we analyze the *ASCA* X-ray emission within a single large aperture for each group which encloses the region of the most significant emission (see below).

We obtained *ASCA* data for the 12 groups from the public data archive maintained by the High Energy Astrophysics Science Archive Research Center (HEASARC). The properties of the observations are listed in Tables 2 and 3. We reduced these data with the standard FTOOLS (v4.2) software according to the procedures described in The *ASCA* Data Reduction Guide and the WWW pages of the *ASCA* Guest Observer Facility (GOF)<sup>†</sup>.

### 2.1 SIS

Most of the SIS data for these groups required corrections and screening in addition to those performed under the standard Revision 2 Data Processing (REV2). Many of these observations were taken after 1994 at which time the effects of radiation damage on the SIS CCDs began to become important (see Dotani et al. 1995). One of the problems caused by radiation damage is the Residual Dark Distribution (RDD) which is essentially an increase in the dark current of the CCDs (see <http://www.astro.isas.ac.jp/~dotani/rdd.html>). RDD degrades the energy resolution and the detection efficiency of the data.

Although in principle one can correct for the RDD effect, the presently available RDD maps and software (i.e. FTOOL CORRECTRDD) do not fully restore the SIS data for energies below  $\sim 0.8$  keV. The primary result is that the SIS data overestimate the column density by  $\sim 2 \times 10^{20}$  cm<sup>-2</sup>, an effect which is more serious for the SIS1 (see the *ASCA* GOF WWW pages). This excess column is of similar magnitude to the Galactic columns of the groups in our sample (see Table 2).

The most accurate correction for the RDD effect is possible for SIS data taken in FAINT mode. After applying the RDD correction the FAINT mode data is converted to BRIGHT2 mode data for which spectral responses can be generated using the standard software. Unfortunately, for several of the observations the exposures were approximately evenly split between FAINT mode and BRIGHT mode.

<sup>†</sup> See <http://heasarc.gsfc.nasa.gov/docs/asca/abc/abc.html> and <http://heasarc.gsfc.nasa.gov/docs/asca/>.

**Table 1.** Group and BGG Properties

Group	$z$	$N_{\text{gal}}$	$\sigma$ (km s <sup>-1</sup> )	$N_{\text{H}}$ (10 <sup>21</sup> cm <sup>-2</sup> )	$\log_{10} L_x$ (erg s <sup>-1</sup> )	BGG Name	Type	$B_{\text{T}}^0$	$\log_{10} L_B$ (erg s <sup>-1</sup> )
HCG 51	0.0258	...	240	0.12	42.40	NGC 3651	E1	14.49	43.18
HCG 62	0.0146	45	376	0.27	42.20	NGC 4761	S0	13.30	43.16
MKW 9	0.0397	...	336	0.39	42.73	UGC 09886	S0	14.29	43.63
NGC 533	0.0181	36	464	0.32	42.31	same	E3	12.22	43.78
NGC 1132	0.0232	...	253	0.48	42.48	same	E	13.01	43.68
NGC 2563	0.0163	29	336	0.43	41.76	same	S0	13.01	43.37
NGC 4104	0.0283	...	546	0.17	42.52	same	S0	12.93	43.88
NGC 4325	0.0252	18	265	0.23	42.91	same	E4	14.41	43.19
NGC 5129	0.0233	33	294	0.18	42.09	same	E	12.89	43.73
NGC 5846	0.0061	20	368	0.42	41.90	same	E0-1	11.13	43.47
NGC 6329	0.0276	...	...	0.21	42.07	same	E	13.62	43.59
RGH 80	0.0370	...	448	0.10	42.74	...	...	...	...

Properties for the groups and their brightest group galaxy (BGG); i.e. morphological types, blue magnitudes, and blue luminosities refer to the BGG. Redshifts are taken from NED and the RC3. The number of group galaxies ( $N_{\text{gal}}$ ) and velocity dispersions ( $\sigma$ ) are taken from Zabludoff & Mulchaey (1998) for six galaxies. Velocity dispersions for other galaxies are from Hickson et al. (1992) for HCG 51 and 62, from Beers et al. (1995) for MKW9 and NGC 4104, from Tonry & Davis (1981) for NGC 1132, and from Ramella et al. (1995) for RGH 80. Galactic Hydrogen column densities ( $N_{\text{H}}$ ) are from Dickey & Lockman (1990) using the HEASARC w3nh tool. The X-ray luminosities,  $L_x$ , are computed in the 0.5-10 keV energy band from the (unabsorbed) 2T models in section 3.2.2 of this paper. The distances used for these calculations are obtained from the quoted redshifts with  $H_0 = 70$  km s<sup>-1</sup> Mpc<sup>-1</sup> except for the nearby galaxy NGC 5846 for which use the distance from Faber et al. (1989) rescaled for  $H_0 = 70$  km s<sup>-1</sup> Mpc<sup>-1</sup>. Morphological types and total apparent blue magnitudes ( $B_{\text{T}}^0$ ) for the BGGs are from the RC3. The blue-band luminosities of the BGGs are computed from  $B_{\text{T}}^0$  using the distances as above and  $L_{B\odot} = 4.97 \times 10^{32}$  erg s<sup>-1</sup>.

**Table 2.** ASCA Observations

Group	Sequence	Date Mo/yr	SIS	SIS	RDD	Default Screen	SIS Temp		SIS BKG	Radius (arcmin)		Radius (kpc)	
			CCD Mode	Data Mode	Correct		S0 (°C)	S1 (°C)		SIS0	GIS	SIS0	GIS
HCG 51	82028000	6/94	1+2	B	N	Y	...	...	T	3.9	4.5	125	145
HCG 62	81012000	1/94	2	B	N	Y	...	...	T	3.0	3.5	55	64
MKW 9	83009000	2/95	2	B	Y	N	-61.0	-60.8	L	4.0	4.4	198	218
NGC 533	62009000	8/94	4	B	N	N	-59.5	-59.0	L	3.5	3.5	79	79
	62009010	1/96	2	B	Y	N	-59.5	-59.0	L	3.5	3.5	79	79
NGC 1132	65021000	8/97	1	B	Y	Y	...	...	T	3.8	4.5	110	130
NGC 2563	63008000	10/95	1	F	Y	Y	...	...	T	3.0	3.4	61	69
NGC 4104	83008000	12/94	2	B	N	N	-60.5	-60.0	T	3.0	4.0	106	141
	84017000	5/96	1	F	Y	N	...	-61.0	T	3.0	3.4	106	120
NGC 4325	85066000	1/97	2	F	Y	Y	...	...	T	3.0	3.4	94	107
NGC 5129	84048000	7/96	2	B	Y	Y	...	...	T	3.0	3.5	87	102
NGC 5846	61012000	2/94	4	B	N	N	...	...	L	4.1	4.5	55	60
NGC 6329	84047000	4/96	2	B	Y	Y	...	...	T	3.0	3.4	103	117
RGH 80	83012000	6/95	2	B	Y	Y	...	...	T	3.6	3.8	166	175

See text in section 2 for explanation of the terminology used in this table. Additional information for some individual groups is given at the end of the section. Distances computed as described in notes to Table 1.

Since the spectral responses of BRIGHT and BRIGHT2 mode data are different, the data from these different modes cannot be combined. However, the FAINT mode data instead can be converted to BRIGHT mode data (as is done in the standard processing), and this BRIGHT mode data can be corrected for the RDD effect.

Since the benefit from larger S/N outweighs the small improvement in the RDD correction for FAINT mode data, for groups that require the RDD correction but have a significant fraction of their exposure taken in BRIGHT mode, we performed the RDD correction on the BRIGHT mode data: i.e. both on the real BRIGHT data and the BRIGHT data that is converted from FAINT mode. For other groups that require the RDD correction, we applied the correction on the FAINT mode data which is then converted to BRIGHT2 for further analysis. Finally, we analyzed the BRIGHT mode

data for all groups that do not require RDD correction. (As is standard only data taken in medium and high bit rates were used for the SIS.)

Most of the events files were filtered using the default REV2 screening criteria. The most frequent departure from the default screening occurred because of temperature fluctuations in the SIS. The data quality, most importantly the energy resolution, of the SIS CCDs significantly degrades when the temperatures exceed  $\sim -60^\circ\text{C}$ , though optimal performance is achieved for temperatures below  $\sim -61^\circ\text{C}$ . In addition, the maps required for the RDD correction are defined according to 1-degree intervals in the SIS temperature; e.g.  $-61^\circ\text{C}$  to  $-62^\circ\text{C}$ . The current software allows the RDD correction to be made with only one RDD map for each SIS. We defined maximum temperatures considering these issues. In Table 2 we list the maximum temperatures

**Table 3.** *ASCA* Exposures and Count Rates

Name	Sequence #	Exposure ( $10^3$ s)		Count Rate ( $10^{-2}$ ct s $^{-1}$ )		Exposure ( $10^3$ s)		Count Rate ( $10^{-2}$ ct s $^{-1}$ )	
		SIS0	SIS1	SIS0	SIS1	GIS2	GIS3	GIS2	GIS3
HCG 51	82028000	72.0	71.6	5.7	4.6	72.0	72.0	2.2	2.6
HCG 62	81012000	17.2	18.7	10.2	9.5	33.8	33.8	3.5	4.7
MKW 9	83009000	29.0	18.8	8.1	5.9	46.7	46.7	3.9	4.5
NGC 533	62009000	8.9	9.4	5.4	3.4	19.6	19.6	2.7	3.6
	62009010	14.9	14.9	7.4	5.2	18.2	18.2	3.2	3.7
NGC 1132	65021000	30.5	30.5	8.2	6.1	29.5	29.4	2.9	3.6
NGC 2563	63008000	45.8	45.8	2.7	2.0	51.1	50.4	1.1	1.3
NGC 4104	83008000	12.2	11.6	5.8	4.3	45.8	45.8	3.4	4.2
	84017000	21.8	20.9	5.4	4.6	24.7	24.5	2.9	3.5
NGC 4325	85066000	19.7	19.7	18.1	12.7	29.0	29.0	5.4	6.1
NGC 5129	84048000	31.2	29.5	3.0	2.4	34.1	34.1	1.1	1.4
NGC 5846	61012000	24.8	11.5	17.7	9.9	40.4	40.4	4.8	5.4
NGC 6329	84047000	30.9	32.1	3.2	2.7	...	38.3	...	1.8
RGH 80	83012000	39.2	37.6	6.0	4.6	45.2	44.2	1.9	2.4

The count rates are given for energies 0.55-9 keV for SIS data before 1996, 0.65-9 keV after 1996, and 0.8-9 keV for the GIS. The count rates are background subtracted within the particular aperture (see text in section 2).

for each SIS for those observations that required temperature filtering.

We also improved the data quality for a few groups by using more restrictive angles from the bright Earth (BR\_EARTH) and smaller values for the Radiation Belt Monitor (RBM); these occurrences are listed at the end of this section. Our final screening of the data involved visual examination of the light curves for each observation and removing intervals of anomalously high (or low) count rate. Note only data with the standard event grades (0234) were used.

The gain of the SIS varies from chip-to-chip, and the variation is a function of time owing to radiation damage. We have corrected the SIS data for these effects using the most up-to-date calibration files as of this writing (sisph2pi\_110397.fits).

The final processed events were then extracted from a region centered on the emission peak for each detector of each sequence. We selected a particular extraction region using the following general guidelines. Our primary concern is to select a region that encloses most of the X-ray emission yet is symmetrically distributed about the origin of the region; as a result, we used circles for most of our extraction apertures. We limited the size of the aperture to ensure that the entire aperture fit on the detector, an issue more important for the SIS because of its smaller field-of-view (20' square for SIS vs 50' diameter for GIS). Moreover, for the SIS0 and SIS1 we tried to limit the apertures to as small a number of chips as possible to reduce the effects of residual errors in chip-to-chip calibration.

We extracted the events using regions defined in detector coordinates as is recommended in the *ASCA* ABC GUIDE because the spectral response depends on the location in the detector not the position on the sky. The radii for the SIS extraction regions are listed in Table 2. (For NGC 1132 we used a square box for the SIS0 data and a rectangular box for the SIS1 data. The radius listed for this group in Table 2 corresponds to one-half the length of the sides of the SIS0 box. The SIS1 region is obtained by squashing the SIS0 box by 10% along one of the coordinate axes.)

We emphasize that our SIS regions cover the area of significant S/N and are negligibly contaminated by any obvious sources in the field. This contrasts with the procedure of Davis et al. (1999) who defined most of their radii to encircle all of the emission detected with *ROSAT*. Their procedure leads to radii that are factors of 5-10 larger than our values listed in Table 2. However, the *ASCA* data at such large radii are very noisy and do not improve constraints on spectral models obtained from using our smaller regions; i.e. we find that using larger apertures increases the noise and generally loosens constraints on the models obtained using data in the apertures enclosing the highest S/N data.

For most of the observations we computed a background spectrum for each detector using the standard deep observations of blank fields; these are indicated by “T” under “SIS BKG” in Table 2. There are important advantages to using these background templates instead of a local background estimate. First, the templates allow background to be extracted from the same parts of the detector as the source and thus the vignetting and other exposure effects are the same for each; this is not the case for background taken from a different region of the detector as the current software does not allow the required corrections to be made for spectral analysis. Second, as stated above, it is known from *ROSAT* observations of these galaxies that their emission extends over much of the field of view of the SIS and perhaps more (e.g. Mulchaey & Zabludoff 1998).

However, it should be remembered that the background templates are most appropriate for SIS data taken in 4-ccd mode early in the mission. For more recent data taken in 1-ccd or 2-ccd mode, using these background templates can lead to spurious effects particularly for energies above  $\sim 7$  keV where instrumental background dominates the cosmic X-ray background. Systematic errors in the SIS at these high energies are not so important for our study since the constraints on spectral models are dominated by data at lower energies. The integrated spectra of these sources within our apertures are not dominated by background and, as a result, the deduced temperatures and abundances are not overly affected whether the templates or local background are used.

For those sources where the screening differed significantly from the REV2 standard we used a local background estimate. The background regions were chosen to be as far away as possible from the group center and any other sources in the field. The observations using a local background are listed with a “L” under “SIS BKG” in Table 2.

The final screened background-subtracted exposures and count rates are listed in Table 3.

The instrument response matrix required for spectral analysis of ASCA data is the product of a spectral Redistribution Matrix File (RMF) and an Auxiliary Response File (ARF). The RMF specifies the channel probability distribution for a photon (i.e. energy resolution information) while the ARF contains the information on the effective area. An RMF needs to be generated specifically for each SIS of each observation because, among other reasons, each chip of each SIS requires its own RMF and the spectral resolution of the SIS is degrading with time. We generated the responses for each SIS using the FTOOL SISRMG selecting for the standard event grades (0234). Using the response matrix and spectral PI (Pulse Invariant) file we constructed an ARF file with the FTOOL ASCAARF.

The source apertures used for the SIS overlapped more than one chip for several of the observations. In order to analyze the spectra of such regions we followed the standard procedure of creating a new response matrix that is the average of the individual response matrices of each chip weighted by the number of source counts of each chip (i.e. within the source aperture). (Actually, the current software only allows the RMFs to be averaged and then an ARF is generated using the averaged RMF. This is considered to be a good approximation for most sources.) Unfortunately, some energy resolution is lost as a result of this averaging. For the observations of our sources, however, this small energy broadening is rendered undetectable by the statistical noise of the data.

## 2.2 GIS

We analyzed the GIS events files processed by the standard REV2 screening. The only additional screening required for a few observations involved removing time intervals with anomalously large deviations from the mean light curve of the data. No dead time corrections were required for the GIS data because the count rates were less than  $1 \text{ ct s}^{-1}$  for each GIS detector for all the observations in Table 3.

For consistency with the SIS data, the regions used to extract the GIS data were chosen to be of similar size to the corresponding SIS regions of a given sequence. Since, however, the GIS+XRT PSF is somewhat larger than that of the SIS+XRT the extraction regions for the GIS are usually  $\sim 20\%$  larger.

The standard observations of blank fields were used to estimate the background for the GIS data. The principal motivation for using these templates for GIS data is that the instrumental background increases rapidly with increasing off-axis angle. We performed the rise-time filtering (i.e. GISCLEAN) on the standard GIS templates as required to match the standard screening. In Table 3 the background-subtracted exposures and count rates are listed for each GIS observation.

The RMFs for the GIS2 and GIS3 are equivalent (and

are assumed to be independent of time), and thus for all GIS spectra we use the GIS RMFs `gis2v4_0.rmf` and its twin `gis3v4_0.rmf` obtained from the HEASARC archive. Using these RMF files an ARF file was generated for each observation.

## 2.3 Comments on individual groups

The observations of several of the groups warrant further discussion.

**HCG 51:** The SIS were operated for  $\sim 45$  ks in 2-ccd mode and for  $\sim 27$  ks in 1-ccd mode. We separately reduced the data for each mode and then combined the source and background spectra, RMFs, and ARFs using the standard software (i.e. with FTOOL ADDASCASPEC v1.27).

**MKW 9:** We adopted slightly stricter screening for the SIS to help compensate for the degradation in data quality arising from the warmer CCD temperatures: i.e. BR\_EARTH  $> 40$  and RBM  $< 50$ .

**NGC 533:** Each SIS for both the 1994 and 1996 observations were unfortunately quite warm for most of the exposures. The maximum temperatures listed in Table 2 represent a compromise between a desire to (1) maximize data quality, (2) maximize the acceptable exposure, and (3) to best match the temperatures of the RDD maps available near the dates of the observations. The maximum temperatures chosen significantly reduced the effective exposure. As a result, since the maximum temperatures still indicate that the data quality are not optimal, we followed the advice in the ASCA ABC guide and increased the acceptable number of events by raising the threshold for pixel rejection to 100 for both SIS of the 1996 observation; for the 1994 observation we raised the threshold to 150 for the SIS0 data and to 200 for the SIS1 data.

Approximately 6 ks of 2-ccd mode data were also taken during 1994. These data were not analyzed since much of the group flux was lost due to the unfortunate placement of the group center near the top edge of the default chips SIS0 chip 1 and SIS1 chip3 (an issue more serious for the SIS1 data). Finally, there is a noticeable point-like source  $\sim 7'$  from the group center. As a result, we limited the sizes of our extraction regions, particularly the GIS because of its larger PSF, to reduce contamination from this source.

**NGC 2563:** Approximately  $7'$  from the group center there is a point-like source.

**NGC 4104 (MKW 4s):** There were two observations taken in 1996. One of the observations only yielded  $\sim 3$ ks of useful exposure when restricting the maximum SIS temperatures to  $-60^\circ\text{C}$  and thus was not included in our analysis.

**NGC 4325:** The shape of the SIS0 spectrum for energies  $\sim 3$ -5 keV is quite sensitive to the size of the region chosen. As the region size is increased from our chosen  $r = 3'$  the spectrum in that energy range flattens significantly. It is possible that an unresolved hard source(s) contaminates the spectrum at larger radii. More likely is that the SIS background template is inadequate for this 1997 observation (see section 2.1). To reduce the sensitivity to either of these issues we choose the minimum region size appropriate for the PSF. This choice is also justified because (1) larger regions centered on the emission peak go off the edge of the SIS, and (2) the emission is very centrally peaked.

**NGC 5129:** There is a fairly bright point-like source  $\sim 7.5'$  from the group center.

**NGC 5846:** We found that the standard REV2 events files produce an SIS0 image having a noticeable excess stream of light on the SIS0 chip 0. As a result, we screened the data ourselves and chose slightly stricter screening criteria: i.e.  $BR\_EARTH > 40, 30$  for the SIS0, SIS1 and RBM  $< 50$  for both SIS.

**NGC 6329:** The GIS2 data between 1-1.5 keV dip significantly, an effect which is much less pronounced in the GIS3 data and not observed with the SIS data. We were unable to affect this behavior in the GIS2 data by changing the screening criteria. Since this dip is likely to be an instrumental effect we exclude the GIS2 data from analysis.

**RGH 80:** There is a fairly bright source  $\sim 7'$  from the group center. We limit the sizes of the regions to reduce contamination from this source.

### 3 BROAD-BAND SPECTRAL FITTING

#### 3.1 Preliminaries

##### 3.1.1 Models

Since the X-ray emission of the groups in our sample is dominated by hot gas, we use coronal plasma models as the basic component of our spectral models. We use the MEKAL plasma code which is a modification of the original MEKA code (Mewe, Gronenschild, & van den Oord 1985; Kaastra & Mewe 1993) where the Fe L shell transitions crucial to the X-ray emission of ellipticals and groups have been recalculated (Liedahl et. al 1995). Although there exist other plasma codes, most notably the popular Raymond-Smith code (1977, and updates), we have shown previously (B99 and BF) that the MEKAL code provides a better description of the ASCA emission of the brightest elliptical galaxies (which are similar to groups) than does the current version of the Raymond-Smith code.

The superiority of the MEKAL code is expected because although both the MEKAL and Raymond-Smith codes are identical in their treatment of the ionization balance as given by Arnaud & Raymond (1992) for Fe and Arnaud & Rothenflug (1985) for the the other elements, the Raymond-Smith code has many fewer lines than does MEKAL, and, more importantly, it does not incorporate the improved calculations of the Fe L shell lines by Liedahl et al. (1995). Despite these differences, qualitatively similar results for ellipticals are usually obtained from the different codes; we refer the reader to section 3.2.2 of B99 for a detailed comparison. For our present investigation we shall employ only the MEKAL code.

We account for absorption by our Galaxy using the photo-electric absorption cross sections according to Balucińska-Church & McCammon (1992). The absorber is modeled as a uniform screen at zero redshift. The column density is generally allowed to be a free parameter to indicate any additional absorption due to, e.g., intrinsic absorbing material, calibration errors, etc. Note, however, that the column density obtained in this manner only estimates the excess absorption because the actual value depends on the details of the absorber; e.g., a patchy intrinsic absorber requires factors for partial covering and the source redshift.

We take solar (photospheric) abundances according to Anders & Grevesse (1989) which give an Fe abundance of  $4.68 \times 10^{-5}$  relative to H by number. Since the meteoritic solar abundances (Fe/H of  $3.24 \times 10^{-5}$  by number) are probably more appropriate, the Fe abundances we quote should be raised by a factor of 1.44 (Ishimaru & Arimoto 1997). We continue to use the photospheric abundances in this paper to facilitate comparison with previous studies.

The simplest spectral model we consider is that of isothermal gas which we refer to as the “1T” model. This model is expressed as  $phabs \times MEKAL$ , where “phabs” represents the absorption and “MEKAL” the thermal plasma emission. The free parameters of this model are the column density,  $N_H$ , the temperature,  $T$ , the metallicity,  $Z$ , and the normalization (emission measure), EM. We focus on models where only the Fe abundance is allowed to be a free parameter and the abundances of all other elements are tied to Fe in their solar ratios; i.e. in this case  $Z$  indicates the Fe abundance. Although the Fe abundance is by far the most important for spectral analysis of the groups in our sample, we also explore models that allow the relative abundances of other elements to be varied separately from Fe.

For the next level of complexity we consider models with two temperatures (2T) which may be expressed as  $phabs_c \times MEKAL_c + phabs_h \times MEKAL_h$ . For these “two-phase” models the first component represents the “colder” gas and the second component the “hotter” gas. The temperatures and columns of each component are free parameters. Similar to the 1T case, we focus on models where the abundances of all the elements of a plasma component are tied to Fe in their solar ratios; i.e. only the metallicity,  $Z$ , is a free parameter. However, we tie together the abundances of the hotter component and those of the colder component. (In no case did we find that relaxing this constraint improved the fits.) In addition we found it useful to explore a model with three temperatures (3T) for some galaxies which is just the obvious extension of the 2T case.

We also consider a multiphase cooling flow model (CF) which provides a simple model for gas emitting over a range of temperatures (Johnstone et al. 1992). This model assumes gas cools continuously at constant pressure from some upper temperature,  $T_{max}$ . The differential emission measure is proportional to  $\dot{M}/\Lambda(T)$ , where  $\dot{M}$  is the mass deposition rate of gas cooling out of the flow, and  $\Lambda(T)$  is the cooling function of the gas (in our case, the MEKAL plasma code). It should be emphasized that this is arguably the simplest model of a cooling flow with mass drop-out. The advantage of this particular model is that it is well studied, relatively easy to compute, and a good fit to several ellipticals (e.g. BF and B99).

Since gas is assumed to be cooling from some upper temperature  $T_{max}$ , the cooling flow model requires that there be a reservoir of gas emitting at temperature  $T_{max}$  but is not participating in the cooling flow. To accommodate this scenario we define our standard multiphase cooling flow model to have two components,  $phabs_c \times CF + phabs_h \times MEKAL_h$ , where the upper temperature of the cooling flow,  $T_{max}$ , and the temperature of the ambient gas,  $T_h$ , are tied together in the spectral fits. We denote this model by “CF+1T”; these CF+1T models thus have one less free parameter than do the 2T models. We also consider the cases where (1) only

the CF component is present, and (2) a plasma component with variable temperature is added.

Finally, for completeness we also consider adding a high-temperature bremsstrahlung component (BREM) to these models to account for possible emission from discrete sources in the central galaxies. Such a component is not expected to be important for groups because of their larger ratios of X-ray to optical luminosity with respect to isolated ellipticals (e.g. Canizares et al. 1987).

### 3.1.2 Calibration and fitting issues

The SIS provides substantially better constraints on the spectral models than the GIS because the superior energy resolution and larger effective area near 1 keV of the SIS allow better measurement of the portion of the spectrum where the bright, temperature sensitive Fe L shell lines dominate the X-ray emission of groups with average temperatures around 1-1.5 keV (e.g. see section 3.1 of B99). In addition, the SIS covers energies down to  $\sim 0.5$  keV as opposed to  $\sim 0.8$  keV for the GIS. Since there exist calibration problems and uncertainties with both the SIS and GIS (see ASCA GOF WWW pages), particularly for energies below 1 keV, we have modified the spectra and fitting procedures accordingly.

As mentioned in section 2.1 radiation damage has reduced the sensitivity of the SIS for energies below 1 keV and has become increasingly important over the past two years. Consequently, for observations taken before 1996 we set the minimum SIS energy to 0.55 keV and raise this to 0.65 keV for later observations. We chose this date based on our previous analysis of the deviations in the SIS0 and SIS1 spectra of the bright elliptical NGC 4636 observed in December 1995 (see Figure 6 of B99).

The GIS has been calibrated using observations of the Crab nebula (Fukazawa et al. 1997). There are some reported problems with the gain of the GIS, although the energy dependence of these problems have not yet been reported (see ASCA GOF WWW pages). Hence, we initially set the lower energy limit for the GIS spectra to 0.8 keV after inspection of the figures in Fukazawa et al. (1997). (Below we revise this choice.)

We decided to analyze SIS and GIS data below 9 keV (similar to B99) because at the highest energies the calibration errors associated with the XRT become increasingly important (Gendreau & Yaqoob 1997), and the background level generally dominates the signal (thus amplifying any errors in the background determination).

Errors in the calibration of the energy scale of the SIS and GIS result in energy offsets of a few eV for the SIS and  $\sim 50$  eV for the GIS (see ASCA GOF WWW pages). To compensate for these systematic errors we follow B99 and allow the redshifts for all detectors of the SIS and GIS to be free parameters. Note that in practice first we determine the best fitting spectral model with the redshifts of the detectors all fixed at their redshifts in Table 1. Then the redshifts are allowed to be free to determine if there is any final improvement in the fits.

All spectral fitting was performed with the software package XSPEC (Arnaud 1996). We used the exact MEKAL models in XSPEC (i.e. model parameter “switch” set to 0), not those derived from interpolating pre-computed tables.

For all fits we used the  $\chi^2$  method implemented in its standard form in XSPEC.

In order for the weights to be valid for the  $\chi^2$  method the PI bins for each source spectrum must be re-grouped so that each group has at least 20 counts. This is generally regarded as the standard binning procedure. The background files also typically have at least 20 counts when their energy bins are grouped similarly to the source spectra. The background-subtracted count rate in a particular group can be small, but the uncertainties in the source and background are correctly propagated by XSPEC to guarantee approximately gaussian statistics for the statistical weights (K. Arnaud 1998, private communication).

As noted by B99 (end of their section 3.1.1), for the brightest ellipticals the standard binning significantly oversamples the energy resolution of both the SIS and GIS, but the effect is more serious for the GIS because it has lower energy resolution than the SIS. The result is that for joint fits of 1T and 2T models to the SIS and GIS data of the brightest ellipticals one obtains values of  $\chi^2$  that are much less than the number of degrees freedom in both cases. Even when the value of  $\chi^2$  is much smaller for the 2T model, both the 1T and 2T models give  $\chi^2$  null hypothesis probabilities  $P \sim 1$ . If, however, the SIS and GIS spectra are re-binned in larger PI groups so that the energy resolution is less oversampled, then the  $\chi^2/\text{dof}$  ratio increases so that  $P$  does distinguish between the 1T and 2T models.

We have verified this sensitivity of  $P$  to the binning for the groups in our sample, though the effect is not so pronounced as for the bright ellipticals studied by B99. From examination of the  $P$ -values obtained from 1T and 2T fits we adopted 40 counts per energy bin for the SIS data and 80 counts per bin for the GIS data for each group. We emphasize that similar to B99 we find no significant changes in the derived model parameters when using the coarser energy binning.

Hence, with the SIS and GIS spectra so prepared initially we fitted the models described in the previous section jointly to the available SIS0, SIS1, GIS2, and GIS3 data for each group. By keeping the data of these detectors separate we were able to assess the importance of calibration differences between the various detectors. In particular, we allowed the column densities and redshifts of each detector to be fitted separately to allow for differences in the low energy responses and the energy scales of the various detectors.

The procedure we follow for spectral fitting is as described in BF and B99. That is, we begin by fitting a 1T model jointly to the spectra; i.e. a single MEKAL model modified by Galactic absorption (see Table 1). The free parameters are the temperature, metallicity, and normalizations of each detector. We then examine whether allowing  $N_{\text{H}}$  to be free significantly improves the fit. For the 2T model we add another temperature component to the best-fitting 1T model with the column density initially tied to the value of the first component; the redshifts and abundances are also tied to those of the first component. Once the new best 2T model is found we allow  $N_{\text{H}}^{\text{h}}$  to vary separately from  $N_{\text{H}}^{\text{c}}$  and fit again to obtain a new best fit. A similar procedure is followed for the other multi-component models.

Upon fitting 1T models to the spectra of each group we found that the column densities for each detector are consistent in essentially every case within their  $1\sigma$  errors; i.e.

the statistical errors on the derived  $N_{\text{H}}$  are larger than the systematic errors due to calibration problems<sup>‡</sup>. This same agreement between detectors is found for  $N_{\text{H}}$  on both components of 2T and CF+1T models for seven of the groups in our sample.

For the other five groups we found that  $N_{\text{H}}^c/N_{\text{H}}^h \gtrsim 1$  for the SIS data but  $N_{\text{H}}^c/N_{\text{H}}^h \ll 1$  for the GIS data. This occurs because the SIS data, which dominates the fits, generally requires both model components to have temperatures near 1 keV. Because the GIS is not as sensitive to energies near 1 keV, the GIS would rather have one component near 1 keV and the other component with a much higher temperature. To accommodate this desire the GIS raises the value of  $N_{\text{H}}^h$  to a very large value ( $\sim$  (several)  $\times 10^{22} \text{ cm}^{-2}$ ) which suppresses the contribution of the hotter temperature component below  $\sim 2$  keV. Then the GIS raises the emission measure of this hotter component to better fit the higher energies. (Note that the improvement in  $\chi^2$  when allowing the column densities of the different detectors to be varied separately is always substantially less than the improvement of, e.g., a 2T model over a 1T model.)

Thus, in order to guarantee qualitative consistency between the different components of the multi-temperature models it is necessary to tie together the column densities between the different detectors. This requirement is further justified by the agreement of the column densities of the different detectors for the 1T models. When tying  $N_{\text{H}}$  between different detectors the measured value simply represents an average. Since the constraints on such an average  $N_{\text{H}}$  provided by the GIS data are dwarfed by the SIS data, and there exist differences in the calibration of the GIS2 and GIS3 below 1 keV that are currently not understood (see Figure 4 of Fukazawa et al. 1997), we raise the minimum energy of the GIS and exclude energies below 1 keV as also done in B99. (We do not notice any significant effect as a result of this choice.)

We also find no significant differences in the measured redshifts between the SIS0 and SIS1 or the GIS2 and GIS3 for any of the groups; i.e. only the redshift differences between the SIS and GIS are important. Hence, it is sensible to further reduce the number of free parameters and tie the together the redshifts of the SIS0 and SIS1 and similarly the GIS2 and GIS3.

Since we intend to tie together  $N_{\text{H}}$  between the different detectors as well as the SIS0/SIS1 and GIS2/GIS3 redshifts, we have eliminated most of the value in analyzing separately the individual detectors of the SIS and GIS. Since S/N is a premium for our analysis we follow B99 and instead analyze the summed SIS=SIS0+SIS1 and summed GIS=GIS2+GIS3 data. The small loss of information resulting from averaging the SIS0 and SIS1 response matrices and the GIS2 and GIS3 ARF files is outweighed by the gain in S/N and the increase in the speed of the spectral fitting afforded by the reduction in the number of data sets.

Since combining the data sets increases the number of

<sup>‡</sup> Since the differences in  $N_{\text{H}}$  between the SIS0 and SIS1 are insignificant the less accurate RDD correction applied to the BRIGHT mode data of some of the observations is unimportant and thus is outweighed by the gain in exposure time (see section 2.1).

counts per PI bin, we slightly increase the PI binning criteria to a minimum of 50 counts for the summed SIS data and to 100 counts for the summed GIS data. Note that similar to B99 we find that the best-fitting parameters obtained from fitting the summed SIS and summed GIS data differ insignificantly from those obtained when fitting all detectors separately (with columns tied between the detectors).

Finally, we emphasize that obtaining the global minimum for the multicomponent models often requires some effort (see BF and B99). Often the fits land in a local minimum upon first adding another component to a model. The typical case is illustrated as follows. Starting with the best 1T model the 2T model is constructed by adding a second temperature component with the abundance of the second component tied to the first component and  $T_{\text{h}}$  set to some value greater than 1 keV. Initially one finds that the best-fitting abundance is small and similar to the 1T case while  $T_{\text{h}} \gtrsim 3$  keV. By resetting the abundance to a large value (e.g. 2 solar) and  $T_{\text{h}}$  to a smaller value near 1 keV a new deeper minimum is generally obtained.

For example, the initial 2T fit to NGC 5129 gives a value of  $\chi^2 = 41.3$  (32 dof) which is an improvement over the 1T value of 47.8 (36 dof). The best fitting abundance is  $0.14Z_{\odot}$  which similar to the 1T value of  $0.13Z_{\odot}$ , and the best-fitting  $T_{\text{h}}$  is 100 keV which is the maximum allowed by the MEKAL model. However, upon resetting  $Z$  and  $T_{\text{h}}$  following the above prescription the fit improves further to  $\chi^2 = 36.1$  and gives best-fitting values  $Z = 0.69Z_{\odot}$  and  $T_{\text{h}} = 1.46$  keV which are significantly different from the initial fit (see section 3.2).

Therefore, after a fit is completed we always reset a subset of the free parameters (especially  $Z$  and  $T_{\text{h}}$ ) and fit again several times until we are satisfied that the minimum is stable. Stepping through the parameters when determining confidence limits also was useful in assessing the stability of the minimum. This is not the most rigorous method to find the global minimum, but it is at present the most convenient way to do it in XSPEC.

## 3.2 Results

In sum: for each galaxy group we analyze the SIS data which are a sum of the SIS0 and SIS1 data, and similarly the GIS data which are a sum of the GIS2 and GIS3 data. The SIS data are restricted to 0.55-9 keV for observations before 1996 and to 0.65-9 keV for observations since 1996. The energy range for the GIS data is 1-9 keV for all observations. Finally, the PI bins are regrouped so that each group has a minimum of 50 counts for the SIS and 100 counts for the GIS.

Table 4 lists the results of fitting 1T, 2T, and cooling flow (CF and CF+1T) models jointly to the SIS and GIS data of each group. Comments on individual groups are given in section 3.2.5.

### 3.2.1 Isothermal models (1T)

In Figure 1 we plot the best-fitting 1T models and residuals corresponding to the results in Table 4 for six of the groups possessing among the best S/N data in our sample. Only the SIS data is shown because of space considerations and since the GIS residuals are not nearly so prominent to the eye



**Table 4.** Spectral Fits

Group	$N_{\text{H}}^{\text{C}}$ ( $10^{21} \text{ cm}^{-2}$ )	$N_{\text{H}}^{\text{H}}$ ( $10^{21} \text{ cm}^{-2}$ )	$T_{\text{c}}$ (keV)	$T_{\text{h}}$ (keV)	$Z$ ( $Z_{\odot}$ )	$\text{EM}_{\text{c}}$ (see notes)	$\text{EM}_{\text{h}}$	$\chi^2$	dof	$P$
HCG 51:										
1T	$0.69^{+0.22}_{-0.20}$	...	$1.35^{+0.05}_{-0.05}$	...	$0.33^{+0.07}_{-0.06}$	$1.74^{+0.18}_{-0.16}$	...	158.3	115	4.6e-3
2T	$3.17^{+1.95}_{-3.17}$	$0.77^{+0.51}_{-0.41}$	$0.68^{+0.15}_{-0.13}$	$1.49^{+0.12}_{-0.09}$	$0.54^{+0.18}_{-0.12}$	$0.34^{+0.42}_{-0.26}$	$1.23^{+0.27}_{-0.18}$	137.1	111	4.7e-2
CF+1T	$2.92^{+0.94}_{-2.09}$	$0.59^{+0.99}_{-0.59}$	$1.54^{+0.17}_{-0.12}$	tied	$0.58^{+0.24}_{-0.16}$	$7.15^{+4.09}_{-4.36}$	$0.86^{+0.43}_{-0.37}$	138.1	112	4.8e-2
HCG 62:										
1T	$0.00^{+0.27}_{-0.00}$	...	$1.07^{+0.04}_{-0.04}$	...	$0.21^{+0.04}_{-0.04}$	$3.48^{+0.41}_{-0.31}$	...	123.9	61	3.5e-6
2T	$1.32^{+1.36}_{-1.32}$	$1.44^{+1.41}_{-1.44}$	$0.69^{+0.06}_{-0.05}$	$1.44^{+0.27}_{-0.16}$	$0.99^{+0.94}_{-0.38}$	$0.69^{+0.59}_{-0.38}$	$1.24^{+0.50}_{-0.45}$	63.3	57	0.26
CF	$1.78^{+0.41}_{-0.49}$	...	$1.69^{+0.18}_{-0.12}$	...	$0.82^{+0.39}_{-0.22}$	$7.90^{+1.72}_{-1.77}$	...	70.8	61	0.18
MKW 9:										
1T	$1.38^{+0.44}_{-0.41}$	...	$2.16^{+0.15}_{-0.14}$	...	$0.45^{+0.15}_{-0.12}$	$2.35^{+0.27}_{-0.24}$	...	110.0	92	9.8e-2
2T	$4.72^{+1.98}_{-2.97}$	$3.14^{+1.26}_{-1.23}$	$0.65^{+0.15}_{-0.12}$	$2.30^{+0.27}_{-0.22}$	$0.70^{+0.31}_{-0.22}$	$0.56^{+0.68}_{-0.39}$	$2.15^{+0.39}_{-0.34}$	89.7	88	0.43
CF+1T	$2.28^{+1.64}_{-2.28}$	$2.81^{+1.91}_{-1.54}$	$2.42^{+0.59}_{-0.33}$	tied	$0.57^{+0.24}_{-0.17}$	$8.29^{+8.77}_{-6.51}$	$1.87^{+0.65}_{-0.90}$	94.2	89	0.33
NGC 533:										
1T	$0.00^{+0.60}_{-0.00}$	...	$1.26^{+0.06}_{-0.09}$	...	$0.27^{+0.09}_{-0.07}$	$1.95^{+0.38}_{-0.25}$	...	90.1	64	1.8e-2
2T	$2.94^{+2.16}_{-2.94}$	$2.82^{+1.34}_{-2.04}$	$0.63^{+0.09}_{-0.10}$	$1.37^{+0.29}_{-0.18}$	$1.16^{+6.84}_{-0.67}$	$0.46^{+0.81}_{-0.39}$	$0.90^{+0.80}_{-0.66}$	68.5	58	0.16
CF+1T	$2.77^{+0.84}_{-2.77}$	$0.73^{+3.42}_{-0.73}$	$1.56^{+0.19}_{-0.31}$	tied	$0.80^{+0.88}_{-0.36}$	$7.31^{+3.55}_{-2.59}$	$0.38^{+1.08}_{-0.32}$	73.5	59	9.7e-2
NGC 1132:										
1T	$0.02^{+0.45}_{-0.02}$	...	$1.15^{+0.04}_{-0.05}$	...	$0.26^{+0.06}_{-0.05}$	$2.20^{+0.30}_{-0.22}$	...	71.2	69	0.40
2T	$3.87^{+2.07}_{-3.10}$	$0.00^{+0.63}_{-0.00}$	$0.71^{+0.19}_{-0.18}$	$1.31^{+0.17}_{-0.11}$	$0.57^{+0.41}_{-0.22}$	$0.92^{+0.93}_{-0.66}$	$1.18^{+0.63}_{-0.43}$	67.7	65	0.39
CF+1T	$3.40^{+2.21}_{-3.40}$	$0.00^{+3.17}_{-0.00}$	$1.22^{+0.14}_{-0.09}$	tied	$0.43^{+0.40}_{-0.17}$	$13.05^{+8.70}_{-12.15}$	$1.10^{+0.49}_{-0.66}$	68.9	66	0.38
NGC 2563:										
1T	$0.85^{+0.47}_{-0.41}$	...	$1.35^{+0.11}_{-0.10}$	...	$0.36^{+0.15}_{-0.11}$	$0.76^{+0.16}_{-0.14}$	...	68.0	60	0.22
2T	$4.36^{+2.03}_{-4.36}$	$0.40^{+2.18}_{-0.40}$	$0.80^{+0.18}_{-0.13}$	$1.81^{+0.49}_{-0.36}$	$0.91^{+1.01}_{-0.45}$	$0.29^{+0.34}_{-0.23}$	$0.30^{+0.31}_{-0.13}$	52.5	56	0.61
CF+1T	$3.37^{+0.39}_{-2.19}$	$0.00^{+4.97}_{-0.00}$	$1.81^{+0.52}_{-0.30}$	tied	$0.90^{+0.67}_{-0.38}$	$2.12^{+0.34}_{-1.28}$	$0.10^{+0.39}_{-0.10}$	53.5	57	0.61
NGC 4104:										
1T	$0.12^{+0.29}_{-0.12}$	...	$2.15^{+0.13}_{-0.13}$	...	$0.57^{+0.16}_{-0.14}$	$1.43^{+0.17}_{-0.15}$	...	131.7	109	6.9e-2
2T	$2.73^{+2.37}_{-2.73}$	$1.12^{+1.17}_{-0.98}$	$0.76^{+0.23}_{-0.17}$	$2.30^{+0.38}_{-0.26}$	$0.70^{+0.32}_{-0.25}$	$0.32^{+0.38}_{-0.21}$	$1.11^{+0.26}_{-0.20}$	109.7	103	0.31
CF+1T	$2.23^{+0.53}_{-0.54}$	$0.00^{+3.17}_{-0.00}$	$3.10^{+0.32}_{-0.40}$	tied	$0.71^{+0.26}_{-0.20}$	$5.54^{+1.80}_{-1.55}$	$0.35^{+0.39}_{-0.25}$	114.2	104	0.23
NGC 4325:										
1T	$0.96^{+0.52}_{-0.43}$	...	$0.85^{+0.04}_{-0.04}$	...	$0.21^{+0.04}_{-0.03}$	$5.29^{+0.61}_{-0.53}$	...	112.8	89	4.5e-2
2T	$3.17^{+0.80}_{-0.86}$	$0.22^{+0.92}_{-0.22}$	$0.66^{+0.05}_{-0.07}$	$1.09^{+0.14}_{-0.11}$	$0.44^{+0.20}_{-0.11}$	$3.58^{+1.12}_{-1.14}$	$1.27^{+0.83}_{-0.41}$	83.6	85	0.52
CF+1T	$3.42^{+0.52}_{-0.67}$	$1.42^{+1.08}_{-1.07}$	$0.97^{+0.12}_{-0.07}$	tied	$0.48^{+0.28}_{-0.15}$	$74.53^{+21.22}_{-22.56}$	$1.13^{+1.04}_{-0.93}$	88.6	86	0.40
NGC 5129:										
1T	$0.00^{+1.11}_{-0.00}$	...	$0.92^{+0.05}_{-0.10}$	...	$0.13^{+0.04}_{-0.03}$	$1.05^{+0.32}_{-0.15}$	...	47.8	36	9.0e-2
2T	$2.62^{+1.48}_{-2.61}$	$0.00^{+4.21}_{-0.00}$	$0.68^{+0.10}_{-0.09}$	$1.46^{+0.88}_{-0.40}$	$0.69^{+4.10}_{-0.41}$	$0.42^{+0.53}_{-0.37}$	$0.24^{+0.34}_{-0.24}$	36.1	32	0.28
CF	$2.29^{+1.48}_{-0.98}$	...	$1.37^{+0.37}_{-0.28}$	...	$0.58^{+0.58}_{-0.25}$	$7.96^{+9.76}_{-3.04}$	...	37.9	36	0.38
NGC 5846:										
1T	$1.79^{+0.74}_{-0.58}$	...	$0.68^{+0.04}_{-0.04}$	...	$0.26^{+0.12}_{-0.06}$	$5.59^{+0.77}_{-0.67}$	...	178.0	79	1.3e-9
2T	$2.69^{+1.04}_{-0.64}$	$0.00^{+0.79}_{-0.00}$	$0.61^{+0.03}_{-0.03}$	$2.52^{+1.09}_{-0.54}$	$1.15^{+1.12}_{-0.44}$	$1.87^{+0.98}_{-0.81}$	$0.41^{+0.15}_{-0.12}$	98.8	75	3.4e-2
CF	$1.88^{+0.64}_{-0.37}$	...	$1.11^{+0.09}_{-0.13}$	...	$0.43^{+0.14}_{-0.11}$	$3.28^{+1.56}_{-0.65}$	...	137.7	79	4.9e-5
NGC 6329:										
1T	$0.00^{+0.28}_{-0.00}$	...	$1.40^{+0.11}_{-0.10}$	...	$0.21^{+0.10}_{-0.07}$	$1.00^{+0.15}_{-0.13}$	...	34.8	38	0.62
2T	$0.42^{+1.45}_{-0.42}$	tied	$0.72^{+0.30}_{-0.17}$	$1.69^{+0.29}_{-0.21}$	$0.53^{+0.55}_{-0.24}$	$0.10^{+0.12}_{-0.05}$	$0.68^{+0.19}_{-0.18}$	23.4	35	0.93
CF	$1.72^{+0.69}_{-0.68}$	...	$2.41^{+0.46}_{-0.36}$	...	$0.58^{+0.43}_{-0.24}$	$5.15^{+2.04}_{-1.49}$	...	26.2	38	0.93
RGH 80:										
1T	$0.19^{+0.33}_{-0.19}$	...	$1.20^{+0.06}_{-0.06}$	...	$0.26^{+0.06}_{-0.05}$	$1.77^{+0.26}_{-0.22}$	...	125.5	69	3.8e-5
2T	$2.42^{+1.22}_{-1.22}$	$0.00^{+0.42}_{-0.00}$	$0.78^{+0.07}_{-0.06}$	$1.64^{+0.21}_{-0.17}$	$0.67^{+0.42}_{-0.24}$	$0.68^{+0.37}_{-0.25}$	$0.61^{+0.18}_{-0.16}$	79.8	65	0.10
CF	$2.03^{+0.44}_{-0.44}$	...	$1.86^{+0.19}_{-0.08}$	...	$0.89^{+0.38}_{-0.26}$	$23.87^{+5.81}_{-4.94}$	...	102.3	69	5.7e-3

Best-fitting values and 90% confidence limits on one interesting parameter ( $\Delta\chi^2 = 2.71$ ) are listed for isothermal (1T), two-temperature (2T), and multiphase cooling flow models (CF or CF+1T) jointly fit to the SIS and GIS data; the values of  $\chi^2$ , the number of degrees of freedom (dof), and the  $\chi^2$  null hypothesis probability ( $P$ ) are also given. Abundances are quoted in units of their (photospheric) solar values (Anders & Grevesse 1989); i.e. Fe abundance is  $4.68 \times 10^{-5}$  relative to H. For models with multiple temperature components the abundances of the hotter component are tied to the corresponding abundances of the colder component during the fits. For CF+1T models  $T_{\text{h}}$  is tied to  $T_{\text{c}}$  during the fits. The emission measures (EM) are quoted in units of  $10^{-17} n_{\text{e}} n_{\text{p}} V / 4\pi D^2$  similar to what is done in XSPEC except for the CF components where instead  $\text{EM}_{\text{c}}$  refers to  $\dot{M}$  in solar masses per year using the distances described in the notes of Table 1. See section 3.1.1 for further explanation of the models.

**Table 5.** Three-Component Spectral Fits for NGC 5846

$N_{\text{H}}^1$ ( $10^{21}$ cm $^{-2}$ )	$N_{\text{H}}^2$ ( $10^{21}$ cm $^{-2}$ )	$T_1$ (keV)	$T_2$ (keV)	$T_3$ (keV)	$Z$ ( $Z_{\odot}$ )	EM $_1$	EM $_2$	EM $_3$
3T: ( $\chi^2 = 81.0$ , 72 dof, $P = 0.22$ )								
$0.48^{+2.42}_{-0.48}$	$4.42^{+1.30}_{-0.92}$	$0.50^{+0.09}_{-0.18}$	$0.76^{+0.10}_{-0.08}$	$3.27^{+2.86}_{-0.88}$	$3.83^{+\infty}_{-2.53}$	$0.14^{+0.52}_{-0.13}$	$0.55^{+0.82}_{-0.48}$	$0.16^{+0.13}_{-0.06}$
CF+2T: ( $\chi^2 = 82.7$ , 73 dof, $P = 0.20$ )								
$2.23^{+0.89}_{-1.92}$	$5.72^{+8.24}_{-2.04}$	$0.77^{+0.11}_{-0.06}$	tied	$3.72^{+\infty}_{-0.98}$	$2.00_{-0.92}$	$5.70^{+3.52}_{-4.22}$	$0.66^{+0.87}_{-0.44}$	$0.20^{+0.11}_{-0.11}$

Best-fitting values and 90% confidence limits on one interesting parameter ( $\Delta\chi^2 = 2.71$ ) are listed for three-component models jointly fit to the SIS and GIS data of NGC 5846; see Table 4 for additional explanation. The column density of the third component is tied to  $N_{\text{H}}^1$  for the 3T model and is fixed to the Galactic value for the CF+2T model. For the cooling flow model (1)  $T_2$  is tied to the upper temperature of the cooling flow ( $T_1$ ) and (2) EM $_1$  is  $\dot{M}$ .

owing to the poorer energy resolution of the GIS. (We refer the interested reader to B99 for similar plots of the bright elliptical NGC 1399 which show GIS data and residuals.)

In terms of the  $\chi^2$  null hypothesis probability,  $P$ , we find that for most of the groups the 1T models yield fits that are of poor quality or marginal quality ( $P \lesssim 0.1$ ). Inspection of Figure 1 shows that the poor fits are largely the result of the inability to fit the SIS data near 1 keV. These groups all display similar residuals near 1 keV which are analogous to those found for the brightest elliptical galaxies by BF and B99. Notice that NGC 2563 has prominent 1 keV residuals even though  $P = 0.22$ .

Some of the groups have significant residuals at higher energies such as HCG 51, NGC 4325, and NGC 5846. The residual pattern above  $\sim 2$  keV for NGC 5846 clearly indicates emission from a higher temperature component (see section 3.2.2). However, for the other systems the residuals at higher energies probably indicate errors in the background subtraction (see section 3.2.5). We mention that such remaining errors in the background are not very important for our current models because the results do not change appreciably if the energies above  $\sim 3$  keV are excluded from the fits; i.e. the SIS data near 1 keV dominate the fits.

Our conclusion that the 1T models are generally poor fits to the ASCA spectra of these groups is qualitatively consistent with the  $\chi^2$  values (and their implied  $P$ -values) listed in Table 2 of Davis et al. (1999) for several of the groups. (The poor quality of the 1T fits is not discussed by Davis et al.) For other groups, especially HCG 62, NGC 4104, and RGH 80, we obtain substantially smaller  $P$  values. The ability of our spectra to better discriminate between models is not surprising because our spectra are derived from much smaller spatial apertures where the S/N is optimal and contamination from unresolved sources is significantly less important. Moreover, we employ a larger minimum count criterion for grouping the spectral PI bins. (We have discussed the problems with over-sampling the energy resolution of the SIS and GIS in section 3.1.2.)

Most of the fitted column densities are consistent with the Galactic values (Table 1) when considering the SIS calibration uncertainties and, more importantly, the statistical errors. Only MKW 9 and especially NGC 5846 show significant excess absorption, although interpretation in these cases is difficult because the fits are of poor quality. In contrast, some galaxies have best-fitting column densities below the Galactic value which are only marginally consistent within the estimated 90% errors with the Galactic val-

ues (e.g. HCG 62, NGC 1132, NGC 6329). For example, in Figure 1 the 1T model for energies less than 1 keV lies clearly below the data for HCG 62 even with the best-fitting  $N_{\text{H}} = 0$ . Considering that the SIS calibration errors should translate to a measured excess  $N_{\text{H}}$  such examples give additional evidence against the suitability of the 1T model.

The metallicity derived for most of the groups is very sub-solar: for the entire sample we obtain a mean and standard deviation  $\langle Z \rangle = 0.29 \pm 0.12 Z_{\odot}$ . These low abundances are consistent with the previous study of these groups by Davis et al. (1999) who fitted 1T models to the ASCA spectra. Similar low Fe abundances are obtained by Finoguenov et al. (1999) for NGC 5846 and by Finoguenov & Ponman (1999) for HCG 51 and HCG 62 within our apertures. Fukazawa et al. (1998) found similar low Fe abundances for HCG 51, HCG 62, MKW 9, and NGC 4104 (MKW 4s), although their analysis excluded most of the emission at small radii which dominates our apertures. Such sub-solar abundances are also consistent with 1T models fitted to elliptical galaxies (e.g. Matsumoto et al. 1997; BF; B99). However, as we show below in sections 3.2.2, 3.2.3, and Appendix A, these low abundances result from a bias inherent in 1T models.

We have examined models where the  $\alpha$ -process elements O, Ne, Mg, Si, and S are allowed to be varied separately from Fe. Generally the largest improvement in the fits arises from letting the O and Ne abundances go to zero while lesser improvements result when the Si and S abundances take values  $\sim 1.5$ -2  $Z_{\text{Fe}}$ . For most of the groups the improvements in the quality of the fits are insignificant, and for those cases with noticeable increase in  $P$  the improvement is far less than when adding another temperature component as we discuss below.

Similar Si and S enhancements are reported by Fukazawa et al. (1998), Davis et al. (1999), and Finoguenov & Ponman (1999). Since (1) the  $\alpha/\text{Fe}$  ratios are generally poorly constrained and are consistent with solar within the 90% uncertainties, (2) the  $\alpha/\text{Fe}$  ratios, like the Fe abundance, turn out to be highly model dependent (see below and Appendix A), and (3) the 1T models with variable  $\alpha/\text{Fe}$  ratios are in any event still inadequate fits to the data, we do not present detailed results of these models. We refer the interested reader to B99 for detailed exploration of such models for four bright ellipticals for which results entirely analogous to the groups in our sample are obtained.

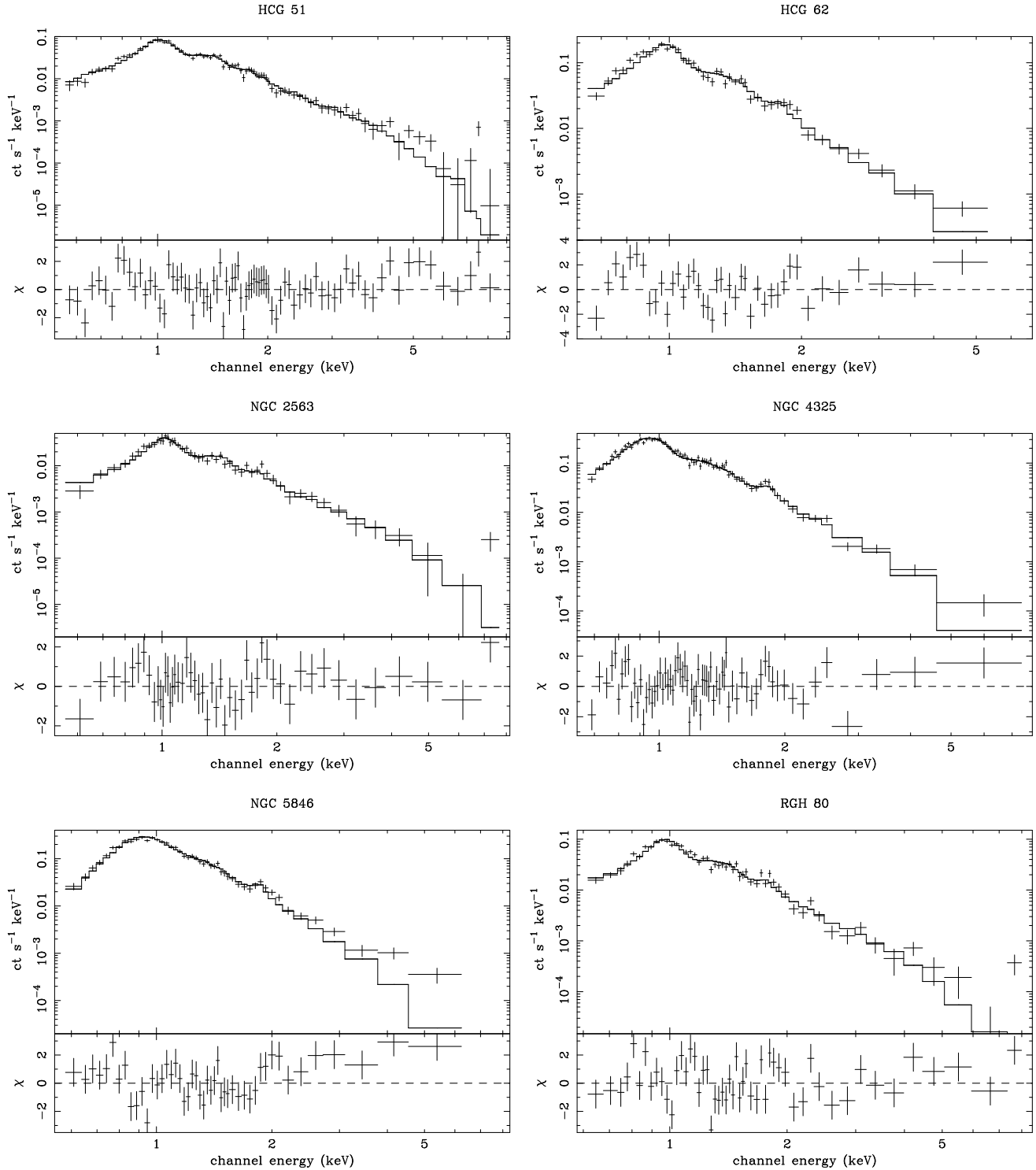


**Figure 1.** Best-fitting isothermal (1T) models jointly fit to the SIS and GIS data for six groups with among the best S/N data in our sample. These models correspond to the 1T results listed in Table 4. Only the SIS data are shown.

### 3.2.2 Two-temperature models (2T)

The 2T models provide significantly better fits than the 1T models to the ASCA spectra of all of the groups in our sample with the exception of NGC 1132. The largest improvements occur for the groups HCG 62, NGC 5846, and RGH 80 which have among the lowest average temperatures and

the best S/N data in our sample. In Figure 2 we display the best-fitting 2T models and residuals for the same groups appearing in Figure 1. Inspection of Figure 2 reveals that with one exception (NGC 5846) the addition of the second temperature component eliminates most of the SIS residuals near 1 keV in a manner analogous to the brightest elliptical galaxies (BF and B99). For NGC 5846 the second temper-

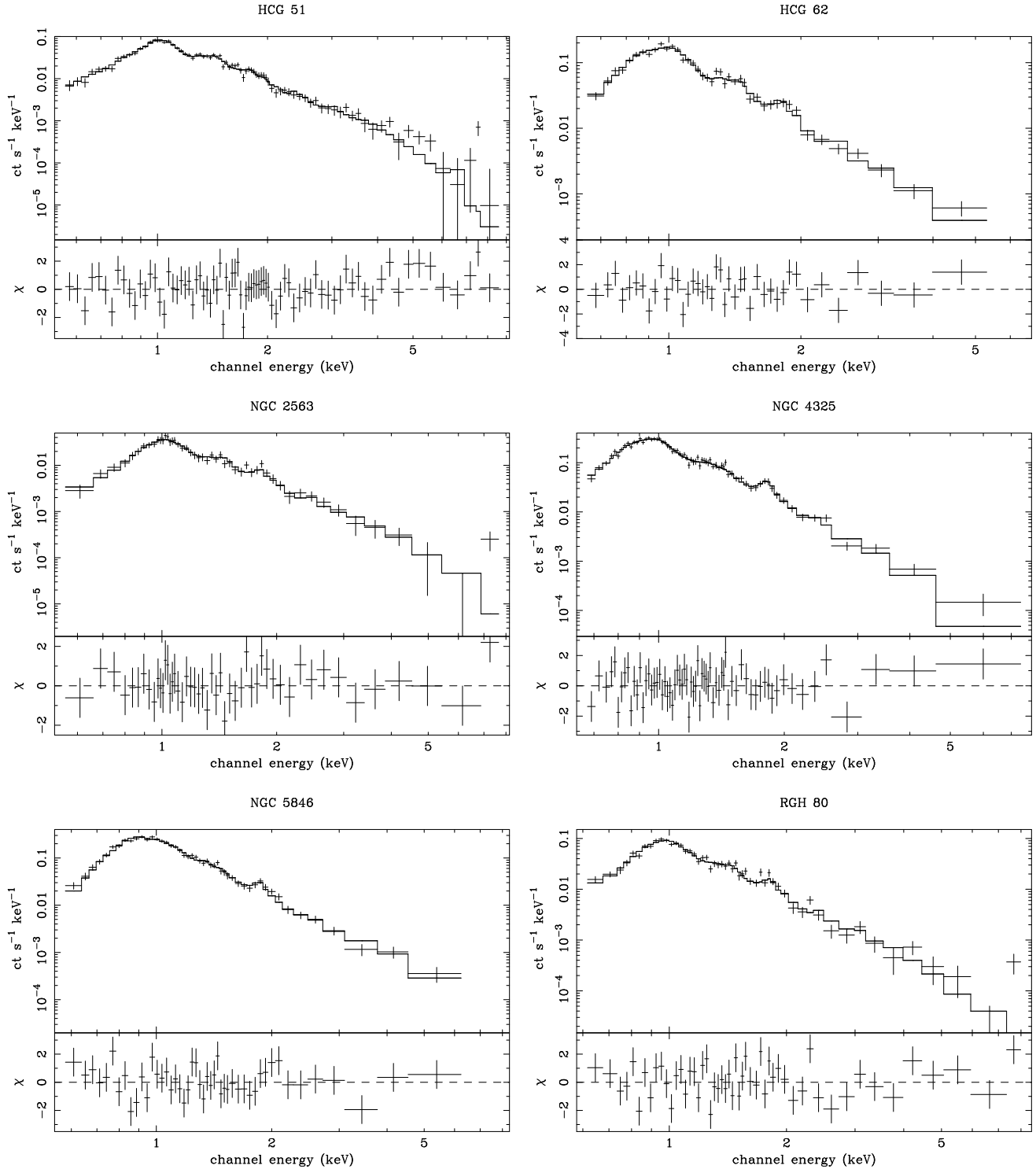


**Figure 2.** As Figure 1 but for two-temperature (2T) models.

ature component largely removes the residuals for energies above  $\sim 2$  keV. We explore in section 3.2.4 whether the addition of a third temperature component can also remove the other SIS residuals for NGC 5846.

Similar to the brightest ellipticals the 2T models also yield values of  $T_h \lesssim 2$  keV which indicate that the second temperature component arises from hot plasma and not the integrated emission from discrete sources in the central

galaxy<sup>§</sup>. For the systems with the lowest average tempera-

<sup>§</sup> For completeness we mention that we have also investigated two-component 1T+BREM models where the temperature of the BREM component is set to a large value  $\sim 10$  keV appropriate for a discrete component as indicated by some studies (e.g. Matsumoto et al. 1997). For every group where the 2T model out-

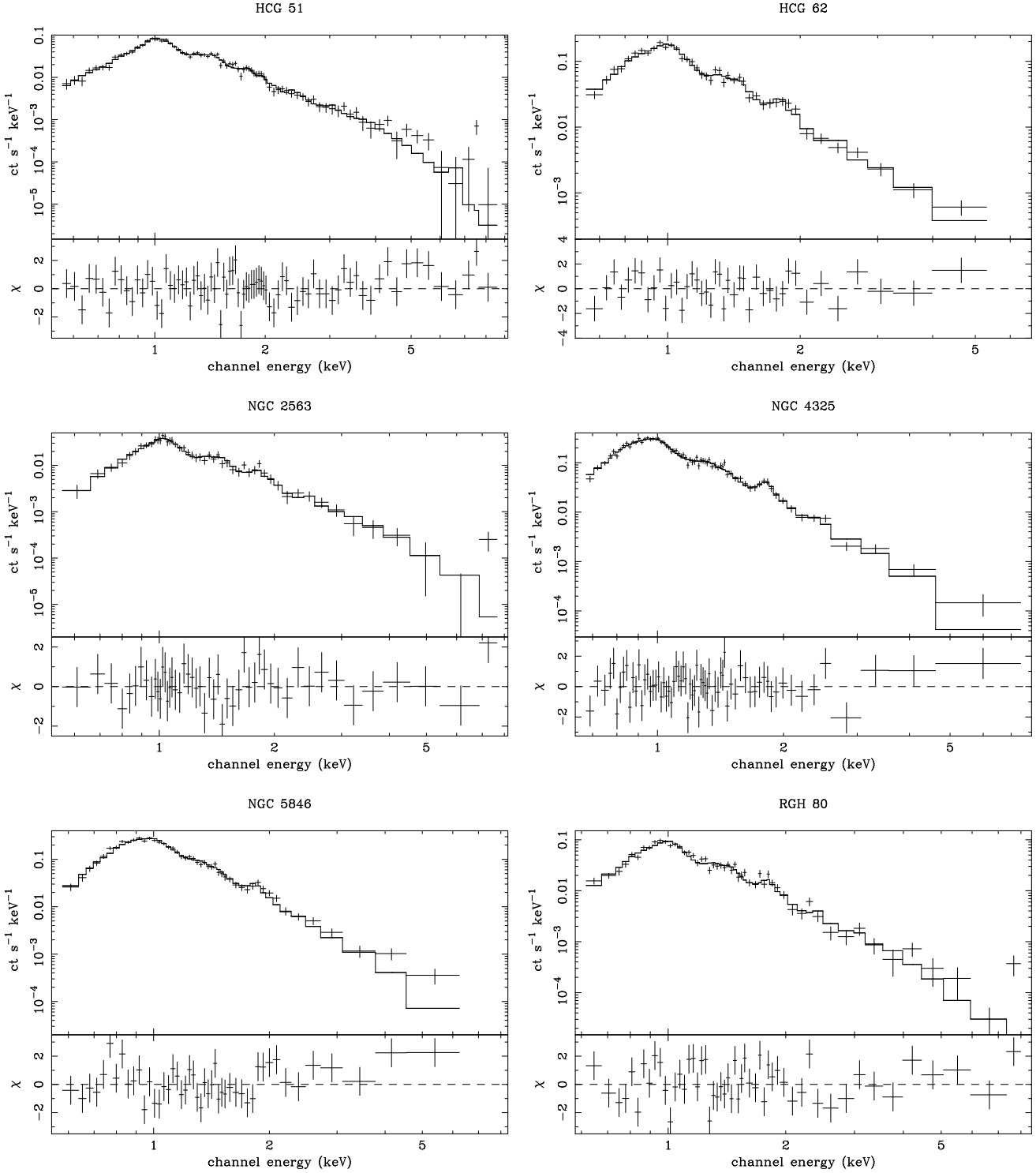


**Figure 3.** As Figure 1 but for multiphase cooling flow (CF or CF+1T) models.

tures we obtain  $EM_h/EM_c \sim 1$  in agreement with the brightest ellipticals (see B99). This ratio increases with tempera-

performed the 1T model we also found that the 2T model fitted substantially better than the 1T+BREM model analogously to the brightest ellipticals studied by B99.

ture such that  $EM_h/EM_c \sim 4$  for the hottest groups in our sample (MKW 9 and NGC 4104).

The results listed in Table 4 for the 2T models apply to fits that allowed the column densities on each component to vary separately (except for NGC 6329 – see section 3.2.5). However, the individual columns are generally poorly constrained for the 2T models. (Note the lower limits on  $N_H^c$  and upper limits on  $N_H^h$  for many of the groups). The im-

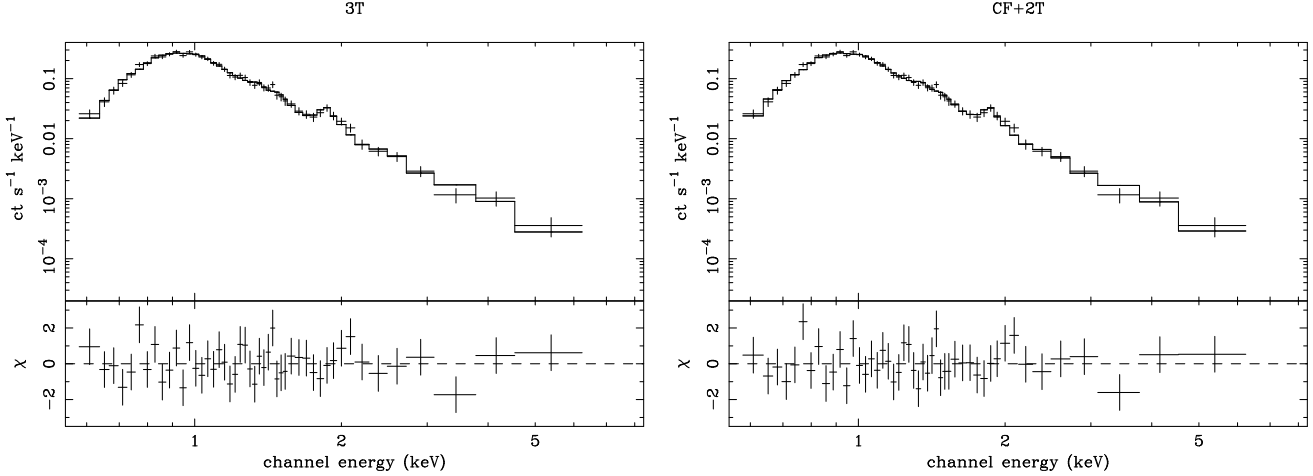


**Figure 4.** Best-fitting three-component (3T and CF+2T) models for NGC 5846 corresponding to those listed in Table 5. Although the models were fit jointly to both the SIS and GIS data, only the SIS data are shown.

provement in the 2T models over the 1T models is not due to the additional degree of freedom associated with allowing both  $N_{\text{H}}^{\text{c}}$  and  $N_{\text{H}}^{\text{h}}$  to be free parameters. The largest improvements are obtained for NGC 4325 and NGC 5846 where  $\chi^2$  decreases by  $\sim 5$  when the column densities are untied in the 2T fits. Finally, we note that the temperatures and abundance do not change substantially when the columns are varied separately.

Despite these uncertainties we present individual constraints on  $N_{\text{H}}^{\text{c}}$  and  $N_{\text{H}}^{\text{h}}$  because for most of the groups the best-fitting  $N_{\text{H}}^{\text{c}}$  exceeds  $N_{\text{H}}^{\text{h}}$ , the latter of which is typically similar to the Galactic value. This systematic trend is equivalent to that found for the brightest elliptical galaxies, though the statistical significance is much greater for the latter (B99). We comment on the origin of the excess absorption in section 4.

The 2T models give metallicities that are substantially larger than the 1T models: for the entire sample we obtain  $\langle Z \rangle = 0.75 \pm 0.24 Z_{\odot}$ ; i.e. the mean is a factor of 2.6 larger than the 1T value. This systematic increase in  $Z$  has also been reported for the brightest ellipticals by BF and B99 and vividly demonstrates the sensitivity of the inferred abundance (particularly Fe) to the assumed temperature structure of the plasma. This systematic effect, or bias, is increasingly more important for the systems with lowest average temperature; e.g., the groups MKW 9 and NGC 4104 which have the largest average temperatures also have the smallest fractional increases in  $Z$  between the 1T and 2T models. We present a detailed discussion of this fitting bias in Appendix A.

We mention that even NGC 1132, which shows no improvement in  $P$  for the 2T model, has a metallicity significantly larger than the 1T value. Moreover, the temperatures, abundance, and other parameters of the 2T model agree very well qualitatively with those of the other groups in the sample; i.e. NGC 1132 displays the same fitting bias as the other groups which strongly suggests that the similarity of its 2T model parameters to the other groups is not accidental.

When allowing the  $\alpha$ -process elements to vary separately from Fe the fits are not improved substantially similar to our results for the 1T models (section 3.2.1). However,

the same abundances which improve the 1T fits also improve the 2T models. Generally, most improvement occurs when  $Z_{\text{O}} \rightarrow 0$ , and although the best-fitting  $Z_{\text{Si}} \rightarrow 1.5\text{--}2 Z_{\text{Fe}}$  for some groups, the Si/Fe ratio does not differ within the estimated  $1\sigma$  errors from 1.

The model dependence of the  $\alpha/\text{Fe}$  ratios is best illustrated with an example. Using 1T models Davis et al. (1999) infer Si/Fe enhancements for some of their groups which are most significant for the hottest groups MKW 9 and NGC 4104. When allowing the  $\alpha$ -process elements to be separately varied from Fe we obtain a best-fitting  $Z_{\text{Si}}/Z_{\text{Fe}} = 1.4$  for the 1T model, which though significantly in excess of 1 is about half the value obtained by Davis et al.. This 1T model also requires zero abundance for O and Mg and does not improve the quality of the fit ( $P = 0.1$ ) over the case where the  $\alpha/\text{Fe}$  ratios are fixed at solar. The 2T model improves slightly ( $P = 0.46$ ) when varying the  $\alpha/\text{Fe}$  ratios, but  $Z_{\text{Si}}/Z_{\text{Fe}}$  does not change significantly from 1. The key improvement arises when letting the O abundance go to zero.

Since the 2T models do not require Si/Fe enhancements for any of the groups in our sample, and the 2T models are clearly favored over 1T models, we conclude that there is no evidence for such enhancements. The inferred peculiar O and Mg abundances inferred by 2T (and 1T) models suggest that further refinement in the absorption model (see 4), model of the temperature structure, plasma code, or calibration is required. We mention that if we instead add another temperature component (i.e. 3T model) with the  $\alpha/\text{Fe}$  ratios fixed at the solar values typically we are able to obtain modest improvements in the fits of comparable magnitude to the models with variable  $\alpha/\text{Fe}$  ratios discussed above (or larger – see below in section 3.2.4).

### 3.2.3 Cooling flow models (CF and CF+1T)

From examination of Table 4 and Figure 3 one sees that the multiphase cooling flow models are substantial improvements over the 1T models and provide fits of comparable quality to the 2T models for all the groups except for NGC 5846 and RGH 80. This similarity to the performance of the 2T models is achieved even though the cooling flow mod-

els have one less free parameter due to the temperatures of the CF and 1T components being tied together (see section 3.1.1). In fact, because the average temperature of the CF component is approximately half the upper temperature (e.g. Buote et al. 1998) the CF+1T models should be similar to 2T models with  $T_c \sim 0.5T_h$  which applies for the majority of the groups in our sample.

For HCG 62, NGC 5129, and NGC 6329 only the CF component is required to produce a fit comparable to the 2T model; i.e. for these groups (and RGH 80) adding the additional 1T component does not improve the fits significantly. Note that two of these groups (NGC 5129 and NGC 6329) have the lowest S/N data in our sample.

In Table 4 the CF model is listed for NGC 5846 even though the CF+1T model yields a better fit with  $P \sim 0.05$ . The primary improvement for the CF+1T model results from allowing the column density on the hotter component to take a huge value ( $N_H^h \sim 10^{24} \text{ cm}^{-2}$ ) which suppresses the 1T component for energies below  $\sim 2 \text{ keV}$  and thus simulates a higher temperature component at larger energies. This effect is related to the SIS and GIS column density discrepancy discussed in section 3.1.2. Note if instead we untie the temperatures of the CF and 1T components then a result analogous to the 2T model is obtained. More complex models for NGC 5846 are considered below in section 3.2.4.

The mass deposition rates ( $\dot{M}$ ) are listed under  $EM_c$  for the cooling flow models in Table 4. We obtain typical  $\dot{M}$  values of 5-10  $M_\odot \text{ yr}^{-1}$  for the groups which lie in between those of giant ellipticals and clusters of galaxies (see Fabian 1994). Outliers include NGC 2563 whose small  $\dot{M}$  is similar to bright ellipticals (e.g. B99) while the large  $\dot{M}$  of NGC 4325 is similar to clusters. The contribution of the CF component to the total emission measure of the CF+1T models is similar to, though somewhat larger than, the contribution of the colder component in the 2T models. This is readily apparent from Table 4 from comparison of the values of  $EM_h$  for the 2T and CF+1T models.

The column densities obtained for the CF+1T models agree very well with those obtained for the 2T models. Similar to the 2T models we also find that the improvement in  $\chi^2$  afforded by separate fitting of  $N_H^c$  and  $N_H^h$  is insignificant in comparison to that obtained when initially adding the second temperature component with  $N_H^c = N_H^h$ . The general trend that  $N_H^c > N_H^h$  where  $N_H^h$  is similar to the Galactic value is consistent with cooling flow models of elliptical galaxies (B99) and clusters of galaxies (e.g. Fabian et al. 1994).

Finally, the metallicities obtained for the cooling flow models systematically exceed those of the 1T models and are similar to those obtained for the 2T models:  $\langle Z \rangle = 0.65 \pm 0.17 Z_\odot$  for the entire sample.

### 3.2.4 Three-component models for NGC 5846

NGC 5846 represents the group whose ASCA spectra are fit the poorest by the 2T and cooling flow models: the 2T model gives only a marginal fit while the cooling flow model is unacceptable (see Table 4). Recall that the addition of the second temperature component of the 2T model largely removes the residuals for energies above  $\sim 2 \text{ keV}$  but does not significantly affect the SIS residuals near 1 keV (Figure 2). In this section we examine whether simple extensions of the

previous models can eliminate the remaining SIS residuals for NGC 5846.

It is possible to reduce the SIS residuals to some extent by varying the  $\alpha/\text{Fe}$  ratios for the 2T model leading to a somewhat better fit ( $P = 0.09$ ). We find for such a model that the best-fitting temperatures, column densities, and Fe abundances do not change when varying the  $\alpha/\text{Fe}$  ratios. In contrast to the other groups (see section 3.2.2) we find that all of the  $\alpha$ -process elements have best-fitting abundances that exceed Fe, although all the ratios except for Ne/Fe are consistent with  $\alpha/\text{Fe}$  of solar within the 90% confidence lower limits.

We can, however, obtain an even better fit keeping the  $\alpha/\text{Fe}$  ratios fixed at their solar values if instead we add another temperature component. In Table 5 we give the best-fitting parameters and their 90% confidence limits for the 3T and CF+2T models; the corresponding best-fitting models and residuals are plotted in Figure 4. For the 3T fits we found that the column densities on the first and third components were similar and not well constrained individually, and so we tied them together. Similarly, for the CF+2T model the column density for the third temperature component turned out to be small and not well constrained, so we fixed it to the Galactic value.

These three-component models are formally acceptable and largely eliminate the SIS residuals near 1 keV similar to the 2T and CF+1T models of the other groups in the sample. The best-fitting metallicities are larger than those obtained for the two-component models but are consistent within the uncertainties. Note in Table 5 that no upper limit is given on  $Z$  for the CF+2T model because the current implementation of the CF model does not allow  $Z > 2Z_\odot$ .

Although the column densities  $N_H^1$  and  $N_H^2$  are not well constrained, both the 3T and CF+2T fits indicate that  $N_H^2 > N_H^1$  in contrast to the two-component models of NGC 5846 and of every other group in the sample. However, similar to the two-component models the separate fitting of the column densities does not improve the 2T or CF+2T model fits very much. For example, if the column densities of each component of the 3T model are tied together the resulting fit is of essentially the same quality,  $P = 0.19$ , although some of the fitted parameters change noticeably: best-fitting  $T_1 = 0.32 \text{ keV}$ ,  $T_3 = 2.5 \text{ keV}$ , and  $Z = 2.7Z_\odot$ . Nevertheless, it is possible that the anomalous  $N_H^2/N_H^1$  ratio reflects complex absorption in NGC 5846, a galaxy with a well-known and prominent dust lane.

The origin of the third temperature component is unclear. It may arise in part from discrete sources in the central galaxy, but the temperature appears to be too low for that to be the only explanation. An intriguing possibility is that it represents an extended intragroup gas component discussed by Mulchaey & Zabludoff (1998). Since the inferred values of  $T_3$  may be too high for gas in hydrostatic equilibrium in the group potential, but are yet too small for discrete sources, the third component may well be a combination of the two effects.

We mention that the other groups do not show as much improvement as NGC 5846 for 3T and CF+2T models because the SIS residuals near 1 keV are already mostly eliminated by the 2T and CF+1T models (sections 3.2.2 and 3.2.3). The marginal fits for a few of the other groups are the result of other residuals (e.g. for HCG 51 at high ener-

gies) that are probably the result of errors in the background subtraction or calibration, though errors in the temperature model and plasma code also may contribute.

### 3.2.5 Comments on individual groups

The spectral fitting of some of the groups require additional comment.

**HCG 51:** If we exclude the energies above 3 keV the fits are improved significantly; e.g.  $P = 0.19$  for the 2T model.

**MKW 9:** The SIS0 and SIS1 data are very inconsistent below 0.7 keV such that models always lie significantly below the SIS0 and above the SIS1 data. As a result we excluded SIS0 and SIS1 data below 0.7 keV.

**NGC 533:** Trinchieri, Fabbiano, & Kim (1997) fitted a 2T model to their *ROSAT* PSPC spectra accumulated within a radius of  $6'$ . Although they tied together the column densities on both components and fixed the Fe abundance at solar, they also found that the 2T model fitted better than an isothermal model and obtained values for  $T_c$  and  $T_h$  in good agreement with ours.

**NGC 1132:** We note that the best-fitting 1T abundance of  $0.58Z_\odot$  obtained by Mulchaey & Zabludoff (1999) using the Raymond-Smith code is about twice the value listed in Table 4. We reproduce their result when using the Raymond-Smith code.

**NGC 5846:** Our 1T and CF models are consistent with those published by BF, but the values of  $T_h$  and  $Z$  for our 2T model are larger than those obtained by BF. Roughly equal contributors to these differences are that BF (1) set  $N_H^c = N_H^h$  and (2) did not include the GIS data in the fits.

**NGC 6329:** Since  $N_H^c$  is unconstrained within the estimated 90% uncertainties we tied together the column densities in the 2T fits.

## 4 DISCUSSION

### 4.1 Properties of the hot gas in groups of galaxies

Previous X-ray studies of groups of galaxies that fitted a single 1T model (e.g. Fukazawa et al. 1998; Davis et al. 1999) or a series of 1T models at different radii (Finoguenov et al. 1999; Finoguenov & Ponman 1999) to the *ASCA* spectra in every case obtained very sub-solar Fe abundances and for many cases obtained Si/Fe ratios in excess of solar. However, we have shown that the *ASCA* spectra accumulated within apertures of  $\sim 3'-5'$  radius (i.e.  $\sim 50 - 200$  kpc) strongly favor multiphase models consisting of at least two temperature components for 11 of the 12 groups in our sample. Moreover, the Fe abundances determined for the multiphase models (2T or cooling flow) are nearly solar and the  $\alpha$ /Fe ratios are consistent with the solar values. Thus, the low Fe abundances and Si/Fe enhancements found by previous studies are an artifact of forcing 1T models to fit the multiphase *ASCA* spectra. This fitting bias is examined in detail in Appendix A.

For several groups in our sample the temperature profiles measured with the *ROSAT* PSPC (e.g. Trinchieri et al. 1997; Mulchaey & Zabludoff 1998) and *ASCA* (Finoguenov et al. 1999; Finoguenov & Ponman 1999) data provide corroborating evidence for multi-temperature hot gas in groups

of galaxies. The temperature profiles are qualitatively similar for each group: starting from a minimum at the center the temperature rises sharply until reaching a maximum at radii of a few arcminutes and then falls gently at larger radii. These temperature maxima occur almost precisely at the edges of the apertures we use to extract the *ASCA* spectra (Table 2); i.e. our apertures include the regions enclosing the positive temperature gradients.

This situation for groups is entirely analogous to that of the brightest ellipticals. B99 showed that the *ROSAT* temperature gradients of the bright ellipticals NGC 1399, NGC 4472, and NGC 5044 are inconsistent with the 1T models obtained from fitting the *ASCA* spectra accumulated within apertures of  $\sim 5'$  radius but are very consistent with two-temperature and cooling flow models. Since the *ROSAT* temperature profiles and *ASCA* multiphase models for the groups are so similar to those of the brightest ellipticals, we refer the interested reader to section 5 of B99 for a detailed demonstration of their consistency. This “equivalence” of a 2T model and temperature gradient was also shown by Trinchieri et al. (1997) for the NGC 533 group using *ROSAT*. As mentioned in section 3.2.5 our 2T model for NGC 533 (Table 4) agrees well with that of Trinchieri et al..

Therefore, very similar to the brightest ellipticals (B99 and BF) the X-ray spectral properties of groups of galaxies can be summarized as follows:

- (i) The hot gas within the *ASCA* apertures ( $\sim 100$  kpc) consists of at least two temperature components.
- (ii) The average temperature is maximum near the edge of the *ASCA* apertures and declines monotonically to a minimum value at the center as indicated by both *ROSAT* and *ASCA* studies.
- (iii) The Fe abundances are  $\sim 0.7Z_\odot$  and the  $\alpha$ /Fe ratios are consistent with their solar values. These abundances represent values averaged over the *ASCA* apertures and thus may reflect abundance gradients within. Though abundance gradients are not required by the current data, the  $Z$ - $R$  correlation discussed in section 4.3 is suggestive of  $Z$  declining with increasing radius.
- (iv) The two-component *ASCA* models suggest absorption in excess of the Galactic value on the colder temperature component while the column density on the hotter component is generally consistent with Galactic. Hence, the excess absorption is concentrated at the center of the group.

Although the measured excess absorption for the groups (sections 3.2.2 and 3.2.3) is not as significant as for the brightest ellipticals (B99) or for clusters of galaxies (e.g. Fabian et al. 1994), the impression is generally the same; i.e.  $N_H^c > N_H^h$  and  $N_H^h$  is similar to the Galactic value. The large values of  $N_H^c$  for ellipticals and clusters imply large amounts of intrinsic absorbing material that generally exceed the amount of cold gas inferred from HI or CO observations of ellipticals (e.g. Bregman, Hogg, & Roberts 1992) and clusters (e.g. O’Dea et al. 1994). Although excess absorption is consistent with the standard multiphase cooling flow models with mass drop-out (e.g. Fabian 1994), this discrepancy between X-ray observations and observations at other wavelengths poses a serious challenge to our understanding of the hot gas in these systems. A detailed exploration of the evidence for excess absorption from X-ray spectral analysis



of ellipticals, groups, and clusters is the subject of a future paper (Buote, in preparation).

#### 4.2 Two-temperature vs. cooling flow models

Similar to the brightest elliptical galaxies the *ASCA* spectra of galaxy groups accumulated within radii of  $\sim 3'-5'$  do not distinguish clearly between two-temperature and simple multiphase cooling flow models; i.e. whether the hot gas emits at only two temperatures or from a range of temperatures cannot be determined presently. This inability of the *ASCA* data to discriminate between 2T and cooling flow models is expected even if the cooling flow models are correct, because the 2T models have an additional free parameter and can approximate very well a cooling flow spectrum throughout the *ASCA* bandpass (Buote et al. 1998). In this section we discuss possible physical scenarios for the two-temperature models and at the end briefly mention the prospects for distinguishing 2T models from cooling flows with future X-ray observations.

The most widely explored two-phase model emphasizes the role of a “hierarchical potential” structure in the hot gas of ellipticals, groups, and clusters. This model ascribes the central enhancements in X-ray surface brightness and central depressions in X-ray temperature to the fact that the central gas sits in the shallower potential well associated with the halo of the cD galaxy while the more extended hotter gas is associated with the gravitational potential of the surrounding group or cluster. In particular, for the clusters of galaxies Hydra-A (Ikebe et al. 1997) and A1795 (Xu et al. 1998) it has been shown that the two-phase models fit the *ASCA* data as well as multiphase cooling flow models. (Typically cooling flow models of clusters also incorporate the influence of the central galaxy on the gravitational potential; e.g. Thomas, Fabian, & Nulsen 1987; White & Fabian 1995)

This “hierarchical potential” model has also been invoked to explain the *ASCA* data of the Fornax cluster which houses the bright elliptical NGC 1399 at its center (Ikebe et al. 1996). However, this two-phase model cannot explain the multi-temperature structure implied by the 2T models obtained by BF and B99 for the *ASCA* data within a radius of  $\sim 5'$ . Firstly, Ikebe et al. assume both components are isothermal. Secondly, the extended component corresponding to the group halo contributes only a small fraction of the emission within a  $\sim 5'$  radius whereas the colder and hotter temperature components obtained by the 2T models of BF and B99 essentially contribute equally to the emissivity. This also applies to the groups in our sample for which Mulchaey & Zabludoff (1998) have found similar two-component structure in the radial distribution of the X-ray emission<sup>¶</sup>.

A two-phase model which can explain the temperature structures implied by the 2T fits to the *ASCA* spectra of the brightest ellipticals and groups is described by Brighenti & Mathews (1998; 1999a). Brighenti & Mathews (1999a) assume that primordial gas at large radii is shock-heated to the virial temperature of the surrounding group potential as the gas flows in to the center during secondary infall.

<sup>¶</sup> It is possible that the third temperature component for the 3T and CF+2T models of NGC 5846 may arise in part from an extended group component (section 3.2.4).

This hotter gas phase is similar to the extended component invoked in the “hierarchical potential” models above. In addition, Brighenti & Mathews account for the mass ejected from stars in the central galaxy during the course of normal stellar evolution. This process continually ejects gas preferentially at the center of the system with a temperature appropriate to the gravitational potential of the central galaxy; i.e. the ejected gas from stellar mass-loss is cooler than the ambient shock-heated primordial gas.

Brighenti & Mathews (1999a) have shown that this two-phase model can accurately reproduce the *ROSAT* temperature and surface brightness profiles of the bright elliptical NGC 4472. Since we demonstrated in B99 that the *ROSAT* temperature gradients for four of the brightest ellipticals (including NGC 4472) are very consistent with the 2T models obtained from fitting the *ASCA* spectra, we conclude that the scenario described by Brighenti & Mathews can also explain the 2T models obtained from fitting the *ASCA* spectra of ellipticals and groups (BF; B99; this paper).

The model of Brighenti & Mathews is a *bona fide* two-phase system whereas the above “hierarchical potential” model is truly single-phase (but not necessarily isothermal) in the sense that a single value of the density and temperature exists at each radius. Although it has no effect on their calculations, it is assumed by Brighenti & Mathews that the stellar ejecta and ambient hot gas mix instantaneously so that a single-phase medium results. However, near the center where the injection of stellar material is most important this may not be the case, and the two phases may co-exist.

In contrast, a continuum of phases is predicted to exist in the cores of ellipticals and clusters in the standard multiphase cooling flow scenario (Fabian, Nulsen, & Canizares 1984; Nulsen 1986, 1998; Thomas et al. 1987; White & Sarazin 1987; see Fabian 1994 for a review). This scenario assumes that in the regions of highest density where the cooling time of the ambient gas is sufficiently short (usually less than the assumed cluster age) gas cools rapidly below X-ray temperatures and drops out of the flow typically with a mass deposition profile  $\dot{M}(< r) \sim r$ . The fate of the cooling gas remains the most serious problem for this scenario (e.g. Fabian 1994), though the cooling gas could provide a natural explanation of the excess absorption obtained from fitting multi-temperature spectral models to the *ASCA* spectra of ellipticals, groups, and clusters. Although excess absorption is not an obvious prediction of the other models described above, Pellegrini & Ciotti (1998) argue that single-phase cooling flows can produce cold gas that would give rise to excess absorption.

It is probably inevitable that aspects of both the two-phase models and multiphase cooling flow scenario operate to some extent in ellipticals, groups, and clusters: i.e. gas cooling out of the hot phase, cool gas ejected from stars in the cD, and hotter gas due to primordial gas shock-heated to the virial temperature of the surrounding group or cluster. Data from future X-ray missions will be able to distinguish between 2T and cooling flow models from spectral fitting within a large spatial aperture (Buote et al. 1998). Moreover, the vastly improved spatial resolution of the *Chandra* and *XMM* satellites over previous missions will allow the location of excess absorbing material and the spatial distribution of distinct gas phases (if present) to be mapped with unprecedented accuracy.

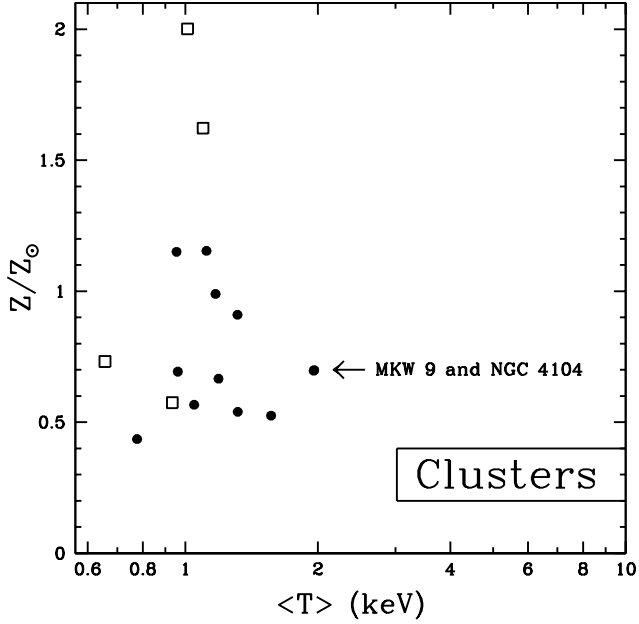


**Figure 5.** The metallicities and the emission-measure-weighted temperatures for ellipticals and groups obtained from two-temperature spectral models. The filled circles represent the groups from this paper while the open squares refer to the bright ellipticals NGC 1399, NGC 4472, NGC 4636, and NGC 5044 analyzed by B99. The region denoted “Clusters” indicates the typical area populated by rich clusters. See section 4.3 for details.

### 4.3 Implications of nearly solar abundances

In Figures 5 and 6 of Renzini (1997) it is shown that the Fe abundances of groups and clusters determined from X-ray observations are much more strongly correlated with temperature than with the luminosity  $L_B$ . For systems above  $T \sim 2$  keV the Fe abundance is approximately constant at  $\sim 0.3Z_\odot$ . Below  $T \sim 2$  keV there is considerable scatter, but most of the systems have  $Z_{\text{Fe}} \lesssim 0.2Z_\odot$ . The Fe abundances quoted by Renzini (1997) were obtained from published isothermal spectral models of the *ROSAT* or *ASCA* data in the literature and therefore suffer from the fitting bias discussed in Appendix A.

We can achieve a more consistent comparison using the 1T models obtained for the groups in our sample. The average metallicity and  $1\sigma$  range for the groups in our sample deduced from 1T models (section 3.2.1),  $\langle Z \rangle = 0.29 \pm 0.12 Z_\odot$ , is very consistent with those obtained for galaxy clusters. Similar to Figure 6 of Renzini (1997),  $Z$  tends to decrease with decreasing temperature for our 1T models. This trend evidently continues below  $\sim 1$  keV since, e.g., BF obtained  $\langle Z \rangle = 0.19 \pm 0.12 Z_\odot$  from 1T fits of a sample of 20 bright ellipticals.

Many have speculated that since  $Z$  correlates with  $T$  below  $\sim 2$  keV, whereas  $Z$  is approximately constant at higher temperatures, there is likely a systematic error affecting the measurement of the Fe abundances. Probably the most frequent suggestion (e.g. Arimoto et al. 1997; Renzini 1997) is that the systematic trend is due to errors in the Fe L lines of the plasma codes, but previously we have shown that existing Fe L errors are not serious for temperature and

abundance determination of normal ellipticals which should be the most affected (BF; B99). Our previous analyses of ellipticals and our current analysis of groups instead demonstrate that the key systematic error in the determination of  $Z$  results from assuming the gas to be isothermal in these systems.

In Figure 5 we plot  $Z$  versus emission-measure-weighted temperature obtained from the 2T models for the groups in our sample; also shown is the region containing most of the cluster  $Z$  measurements as compiled by Renzini (1997). The trend is now quite different from Renzini’s Figure 6 since below  $\sim 2$  keV we find that  $Z$  increases to  $\sim 0.7Z_\odot$  for groups. Unlike the 1T models there is no obvious correlation of  $Z$  with  $\langle T \rangle$  for the 2T models; i.e. removing the “Fe bias” with the 2T models also largely removes the dependence of  $Z$  on temperature for groups.

The 2T models of ellipticals (BF) suggest that  $Z$  may continue to increase for lower temperatures, though the scatter is considerable,  $\langle Z \rangle = 0.9 \pm 0.7 Z_\odot$ . Let us instead focus on the ellipticals NGC 1399, NGC 4472, NGC 4636, and NGC 5044 studied by B99 since they have the best available constraints on the spectral models. Moreover, for NGC 1399, NGC 4472, and NGC 4636 B99 included an emission component that accounts for emission from discrete sources as expected in these systems. The results for these galaxies are plotted as open squares in Figure 5. These objects overlap in temperature with the groups and add extra scatter in  $Z$ .

Since  $Z$  and  $\langle T \rangle$  do not exhibit a strong correlation for the groups and ellipticals we investigate correlations of  $Z$  with other physical quantities. In Figure 6 we plot  $Z$  versus  $L_x$  in the 0.5–10 keV band. There is a significant correlation in the sense that more luminous systems have lower  $Z$ . This trend for groups appears to connect smoothly with clusters ( $Z \sim 0.3Z_\odot$ ) at high  $L_x$ . We mention that similar correlations exist if instead of  $L_x$  we plot  $Z$  against the emission measure of the cooler component (i.e.  $\text{EM}_c \times 4\pi D^2$ ) or  $\dot{M}$  for the cooling flow models; i.e. the trend of decreasing  $Z$  with increasing  $L_x$  (i.e. mass) can also be expressed as  $Z$  decreasing either with increasing luminosity of the cooler component of the 2T models or with increasing mass deposition rate for the cooling flow models.

It is clear from Figure 6 that with respect to X-ray emission the “elliptical” NGC 5044 ( $\log_{10} L_x = 42.74$ ) is more accurately described as a bright group which is also indicated by its large  $\dot{M}$  obtained from a cooling flow model (B99). Also evident is that the elliptical NGC 4636 ( $\log_{10} L_x = 41.53$ ) has smaller  $Z$  than the NGC 1399 and NGC 4472 which have higher  $L_x$ . Of the systems analyzed by B99 NGC 4636 is the only case which required the  $\alpha/\text{Fe}$  ratios to deviate significantly from solar in order to achieve an acceptable fit, and it had the largest contribution from a high energy component presumably arising from discrete sources; i.e. the Fe abundance of NGC 4636 should be regarded as provisional.

The correlation of  $Z$  with  $L_x$  (or with, e.g.,  $\dot{M}$ ) still possesses considerable scatter, and thus there may be other factors to consider. In particular, also in Figure 6 we plot  $Z$  versus  $R$ , where  $R$  is the radius of the circular aperture used to extract the SIS0 spectrum for each object (see Table 2). There is a clear correlation such that the metallicities computed within the largest apertures tend to have the smallest

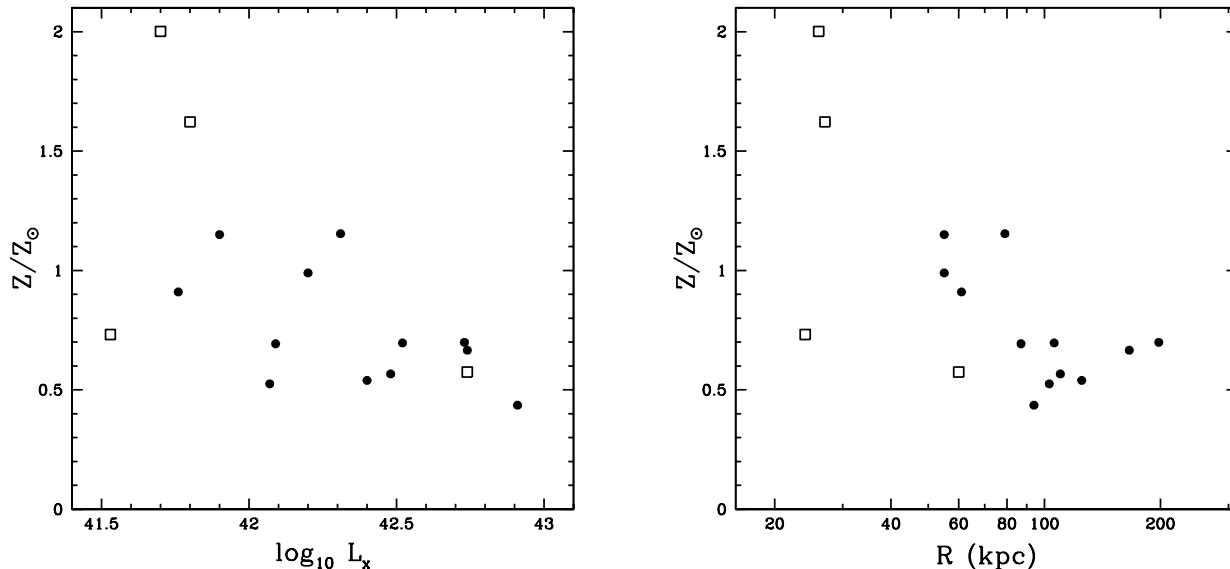


**Figure 6.** As Figure 5 except here we plot the metallicity versus (left) the (unabsorbed) luminosity in the 0.5-10 keV band (see Table 1) and (right) the size of the aperture used for spectral analysis.

values. For  $R \sim 50$ -100 kpc the correlation for the groups has the least scatter; i.e.  $Z$  falls from  $\sim 1Z_{\odot}$  at  $R \sim 50$  kpc to  $\sim 0.5Z_{\odot}$  at  $R \sim 100$  kpc. At larger  $R$  there is no evidence for further decline out to  $R \sim 200$  kpc; i.e. unlike the correlation with  $L_x$  it is not obvious from these data that the  $Z$ - $R$  correlation joins smoothly with clusters.

Nevertheless, this trend of decreasing  $Z$  with  $R$  is consistent with the presence of abundance gradients in these systems. Since  $R$  and  $L_x$  are correlated to some extent because brighter sources generally allow for larger extraction regions, we are unable at this time to determine if the fundamental correlation of  $Z$  is with  $L_x$  or  $R$  or whether they are equally important. From examination of Figure 6 we reach the tentative conclusion that  $Z$  decreases due to increases in both  $R$  and  $L_x$ , but for the groups in our sample abundance gradients are most important for  $R \sim 50$ -100 kpc while the X-ray luminosity is the key determinant for  $\log_{10} L_x \gtrsim 42.5$ . (For the ellipticals NGC 1399, NGC 4472, and NGC 4636 these effects cannot be distinguished.)

Renzini (1997) also shows that the gas fraction ( $f_b$ ) is approximately constant with temperature for clusters but it plummets by several orders of magnitude for temperatures below  $\sim 2$  keV. The determinations of  $f_b$  are not extremely sensitive to  $Z_{\text{Fe}}$  and thus our larger Fe abundances will not change the trend in Renzini's Figure 4 by very much; i.e. the well-known conclusion remains unchanged that the much smaller gas fractions of groups imply that a significant portion of their gas be expelled during their evolution in contrast to clusters.

However, our larger Fe abundances for groups brings these objects into better agreement with the standard chemical models (e.g. Ciotti et al. 1991; Renzini et al. 1993). The previous determinations of very sub-solar  $Z_{\text{Fe}}$  suggested that groups accrete primordial gas at late times after they have already expelled a major portion of their gas as demanded by their low  $f_b$ . The unattractive aspects of this expel-then-accrete scenario are discussed by Renzini (1994; 1997).

The  $\alpha/\text{Fe}$  ratios obtained from our 2T and cooling flow models are consistent with their solar values and those found for the brightest ellipticals (BF; B99). This result taken with the nearly solar Fe abundances indicates that, like clusters, the properties of the hot gas in groups of galaxies are consistent with the standard chemical models; i.e. the Type Ia to Type II supernova ratios and the IMF are similar to those of the Galaxy (see, e.g., Renzini 1997). We note that other chemical models can also produce nearly solar Fe abundances and solar  $\alpha/\text{Fe}$  ratios (e.g. Fujita, Fukumoto, & Okoshi 1997; Brighenti & Mathews 1999b).

## 5 CONCLUSIONS

We have analyzed the ASCA spectra of 12 of the brightest groups of galaxies previously studied by Davis et al. (1999) and Mulchaey & Zabludoff (1999). Because of the limitations inherent in the ASCA PSF we restricted our analysis to the spectra accumulated within a single circular aperture corresponding to radii of  $\sim 3'$ - $5'$  ( $\sim 50$ -200 kpc) for the groups in our sample. Our principal motivation for re-examining these data is to verify whether the very sub-solar Fe abundances obtained from previous studies are in reality an artifact of fitting isothermal models to the X-ray spectra as found for bright elliptical galaxies by BF and B99.

Fitting isothermal models (1T) jointly to the ASCA SIS and GIS spectra gives results that are of poor or at best marginal quality for most of the groups; i.e.  $P \lesssim 0.1$  where  $P$  is the  $\chi^2$  null hypothesis probability. The primary cause of the poor fits is the inability of the 1T models to fit the SIS data near 1 keV. Similar to previous studies these 1T models give very sub-solar metallicities: for the whole sample we obtain a mean and standard deviation  $\langle Z \rangle = 0.29 \pm 0.12 Z_{\odot}$ . Although allowing the  $\alpha$ -process elements to vary separately from Fe often results in  $\alpha/\text{Fe}$  ratios quite different from solar (especially for O and Ne), the quality

of the fits is not improved significantly in most cases. These properties of the 1T fits are very analogous to those of the brightest ellipticals (see B99).

Two-temperature models (2T) provide significantly better fits than the 1T models for 11 out of the 12 groups in our sample. The superior performance of the 2T models arises from their largely removing the residuals in the SIS data near 1 keV present in the fits of the 1T models. For groups where the temperature of the hotter component,  $T_h$ , is  $< 2$  keV the 2T models give  $T_h \approx 2T_c$  where  $T_c$  is the temperature of the colder component in the hot gas. The ratio of emission measures of the two components is  $EM_h/EM_c \sim 1$  for systems with the lowest average temperatures and rises with increasing temperature until  $EM_h/EM_c \sim 4$  for the hottest groups.

Although the column densities on the individual components are not as precisely constrained as those for the brightest ellipticals (B99), the impression is generally the same:  $N_H^c > N_H^h$  and  $N_H^h$  is similar to the Galactic value. We mention that the improvement of the 2T models over the 1T models is not the result of the extra degree of freedom afforded by separately varying  $N_H^c$  and  $N_H^h$ , and the temperatures and Fe abundances do not change substantially either.

The metallicities of the 2T models are considerably larger than obtained for the 1T models,  $\langle Z \rangle = 0.75 \pm 0.24 Z_\odot$ ; i.e. the mean metallicity is a factor of 2.6 larger than the 1T value. Note that the 2T models have the  $\alpha/Fe$  ratios fixed at their solar values. Even if the  $\alpha/Fe$  ratios are allowed to be free parameters, the 2T models do not indicate Si/Fe ratios in excess of solar in contrast to previous studies using isothermal models (e.g. Davis et al. 1999).

We obtain results for the multiphase cooling flow models that are entirely analogous to those of the 2T models including the large metallicities,  $\langle Z \rangle = 0.65 \pm 0.17 Z_\odot$ . Typically the mass deposition rates ( $\dot{M}$ ) are 5-10  $M_\odot \text{ yr}^{-1}$  placing the groups midway between ellipticals and clusters (e.g. Fabian 1994) as expected. Hence, the value of  $\dot{M}$  for the cooling flow models, or equivalently the emission measure of the cooler component for the 2T models, are viable means of distinguishing groups from ellipticals and clusters.

Thus, we have shown that the very sub-solar Fe abundances and Si/Fe enhancements in groups of galaxies found by previous studies (e.g. Davis et al. 1999; Finoguenov & Ponman 1999) are an artifact of fitting 1T models to intrinsically multiphase ASCA spectra. These results are virtually identical to those found for the brightest elliptical galaxies by BF and B99. Owing to the importance of these results for interpreting X-ray spectra, in Appendix A we use simulated ASCA observations to explore in some detail the ‘‘Fe bias’’ and ‘‘Si bias’’ associated with the spectral fitting of ellipticals, groups, and clusters of galaxies.

These fitting biases are not necessarily circumvented if the relatively large circular apertures ( $\sim 100$  kpc) we have used are instead divided into a few annuli, and isothermal models are then fit to the spectra of the annuli; e.g. Finoguenov et al. (1999) and Finoguenov & Ponman (1999). This procedure does not eliminate the fitting bias because the annuli still contain multiple temperature components owing either to the projection along the line-of-sight of different temperature components at radii larger than a given annulus or to the gas being intrinsically multiphase.

It is possible that a strong decrease in metallicity outside of our apertures may in part explain the very sub-solar Fe abundances obtained by Davis et al. (1999) who analyzed the accumulated ASCA spectra within radii that are typically factors of 5-10 larger than ours (Table 2). However, it is doubtful that abundance gradients can give a full accounting of our differences because our  $\sim 100$  kpc apertures enclose a substantial fraction of the emission within the apertures used by Davis et al., yet their very sub-solar Fe abundances obtained with isothermal models agree very well with our isothermal results (Table 4). Also, in section 4.3 we have shown that the apparent flattening of the  $Z$ - $R$  correlation at large  $R$  argues against a substantial decrease in  $Z$  out to radii of at least  $\sim 300$  kpc. Thus, even if  $Z_{Fe} \ll 1Z_\odot$  at radii much larger than our apertures, the ‘‘Fe bias’’ is probably an important contributor to the very sub-solar Fe abundances measured by Davis et al..

We discussed how the properties of the hot gas in groups of galaxies are revised in light of the 2T and cooling flow models, and how the properties are consistently intermediate with those of ellipticals and clusters. Also considered were physical scenarios for the 2T models and how they can be distinguished from cooling flows with future X-ray missions. Finally, we examined the implications of the nearly solar Fe abundances and solar  $\alpha/Fe$  ratios for the groups and how they are consistent with the standard chemical models (e.g. Ciotti et al. 1991; Renzini et al. 1993).

Our results for the brightest ellipticals (BF; B99) and the brightest groups (this paper) demonstrate the similarity of the properties of the hot gas in these systems to cooling flow (i.e. cD) clusters (e.g. Fabian 1994). The different Fe abundances measured for these systems may reflect the sizes of the apertures used for spectral analysis; i.e. the physical aperture size typically used when measuring  $Z_{Fe}$  increases from approximately 30 kpc for ellipticals to 100 kpc for groups up to at least 200-300 kpc for clusters. However, presently the role of abundance gradients cannot be disentangled from that of the X-ray luminosity (or  $\dot{M}$ ) of the system (see section 4.3). Although ellipticals and groups are believed to expel much of their hot gas during their evolution while clusters are ‘‘closed boxes’’ and retain all of their gas, these differences may not much affect the gas properties in their centers, and thus the strong similarity of the gas properties in the cores of these systems is not unreasonable.

The role of abundance gradients in ellipticals, groups, and clusters should be clarified significantly with data from the upcoming *Chandra* and *XMM* satellites which combine high spatial and spectral resolution unlike previous missions.

## ACKNOWLEDGMENTS

This research has made use of (1) ASCA data obtained from the High Energy Astrophysics Science Archive Research Center (HEASARC), provided by NASA’s Goddard Space Flight Center, and (2) the NASA/IPAC Extragalactic Database (NED) which is operated by the Jet Propulsion Laboratory, California Institute of Technology, under contract with the National Aeronautics and Space Administration. The XSPEC implementation of the multiphase cooling flow model was kindly provided by R. Johnstone to whom we express our gratitude. Support for this work was

provided by NASA through AXAF Fellowship grant PF8-10001 awarded by the AXAF Science Center, which is operated by the Smithsonian Astrophysical Observatory for NASA under contract NAS8-39073.

## APPENDIX A: BIASES ASSOCIATED WITH X-RAY SPECTRAL FITTING

The X-ray studies of the hot gas in elliptical galaxies NGC 720 by Buote & Canizares (1994) and NGC 4636 by Trinchieri et al. (1994) were the first to show that the *ROSAT* PSPC spectra of ellipticals could not distinguish between isothermal models with very sub-solar Fe abundances and two-temperature models with solar Fe abundances. Using simulated PSPC data Buote & Canizares (1994) further demonstrated that if the galaxy spectrum is intrinsically characterized by two temperatures with solar Fe abundances but is instead fitted with an isothermal model then sub-solar Fe abundances necessarily result; i.e. the isothermal model gives a strongly biased measurement of the Fe abundance.

The strong dependence of the Fe abundance on spectral model has now been demonstrated using *ASCA* data for elliptical galaxies by BF and B99 and for groups of galaxies in this paper. These papers also show that multiphase models are clearly favored over isothermal models for these systems. As a result, investigators hoping to obtain average Fe abundances for these objects by fitting isothermal models in actuality always infer strongly biased (i.e. very sub-solar) Fe abundances for ellipticals (e.g. Matsumoto et al. 1997) and for groups (e.g. Davis et al. 1999). Since this “Fe bias” is crucial for interpreting the X-ray spectra of these systems, in this Appendix we attempt to elucidate this bias by using simulations of simple multiphase models that are consistent with the current *ASCA* observations of ellipticals, groups, and clusters.

We investigate the dependence of the Fe bias on temperature by considering objects spanning the temperatures of the brightest ellipticals, groups, and clusters of galaxies. In addition, we use *ASCA* simulations of these systems to show the dependence of the  $\alpha$ /Fe ratios on the spectral model. Thus, this Appendix updates and extends the brief studies of the Fe bias that appear in section 2.2 of Buote & Canizares (1994) and in section 3.2.2 of BF.

The key properties of the four reference models we use for this study are listed in Table A1. Each of these models corresponds to regions of positive temperature gradient (e.g. see section 5 of B99). Models 1 and 2 are based on the two-temperature and cooling flow models of the elliptical galaxy NGC 1399 within  $r \sim 30$  kpc (B99) which are also quite similar to the corresponding models of several of the lower-temperature groups in this paper (see sections 3.2.2 and 3.2.3). To explore the high-temperature groups we base model 3 on the cooling flow models of MKW 9 and NGC 4104 (section 3.2.3).

Finally, we obtained the *ASCA* data of A478 from the HEASARC archive and have analyzed the spectra within a  $3'$  radius<sup>||</sup> in a similar manner to the ellipticals and groups

<sup>||</sup> This radius corresponds to 313 kpc assuming a redshift of 0.0882,  $H_0 = 70$  km s<sup>-1</sup> Mpc<sup>-1</sup>, and  $\Omega_0 = 0.3$ .

(see section 2): the result is listed as model 4 and is consistent with previous studies (e.g. Johnstone et al. 1992). A478 was selected because (1) it is one of the brightest clusters having evidence for substantial excess absorption and (2) with respect to other cooling flow clusters a comparatively large fraction of the emission measure arises from the cooling flow component; i.e. A478 should be one of the most favorable clusters for examining systematics when fitting an isothermal model.

We simulated *ASCA* observations of the models in Table A1 using XSPEC. Because of its better energy resolution and sensitivity near 1 keV we focus on the SIS data. For consistency of presentation we use the same PI grouping for each simulated SIS spectrum (i.e. that of the SIS data of NGC 1399 – see B99). Our choices of exposure times for the simulations are motivated by a desire to insure (1) sufficiently high S/N for each case so that noise does not noticeably affect the fitted parameter values, (2) that the sizes of the residuals (in terms of  $\chi^2$ ) are similar to the best available *ASCA* data, and (3) that the simulated data for each model have similar S/N. Although background is included in the simulations, the S/N criteria stated above insure that its effect is only noticeable at the highest energies which are not of interest to our study.

### A1 The Fe bias

In Figure A1 we plot the simulated *ASCA* SIS data of models 1 and 2 from Table A1 and also show the best-fitting isothermal model and its residuals. These 1T models with the  $\alpha$ /Fe ratios fixed at solar give best-fitting values of  $Z = 0.27Z_\odot$  for the simulated 2T model and  $Z = 0.32Z_\odot$  for the simulated CF+1T model. (These metallicities do not differ significantly from the Fe abundances obtained when the  $\alpha$ /Fe ratios are allowed to vary in the fits – see Table A2.) Notice that both the pattern of residuals and the metallicities derived from the 1T fits are very similar for both models 1 and 2 and thus the Fe bias is essentially the same for isothermal fits to two-temperature and cooling flow spectra.

This Fe bias is insensitive to the presence of excess absorption on the colder component. If instead we consider a model identical to model 1 but with  $N_{\text{H}}^c = N_{\text{H}}^h = 5 \times 10^{20}$  cm<sup>-2</sup>, then the metallicity obtained from fitting the 1T model to the simulated *ASCA* data has a best-fitting value  $Z = 0.25Z_\odot$  which is consistent with the value obtained from the simulated model 1 within the  $1\sigma$  errors. Below 1 keV the pattern of residuals for this model differs from model 1 such that the residual peak below 1 keV is slightly less pronounced than in Figure A1.

The pattern of residuals of model 3 (Figure A2) is less complex than for the lower temperature models 1 and 2. The best-fitting metallicity using the 1T model ( $\alpha$ /Fe fixed at solar) is  $0.61Z_\odot$  which represents only a 40% under-estimate of the true value in contrast to the  $\sim 70\%$  under-estimate observed for models 1 and 2. The Fe bias decreases more dramatically as we move to still higher temperatures with model 4 (Figure A2). For this model we obtain a best-fitting value of  $Z = 0.30Z_\odot$  using the 1T model ( $\alpha$ /Fe fixed at solar) which is only a 10% under-estimate of the true value. If we allow the  $\alpha$ /Fe ratios to vary (Table A2) the best-fitting Fe abundance rises to  $0.33Z_\odot$ ; i.e. the Fe bias for hot clusters is insignificant.

**Table A1.** Models

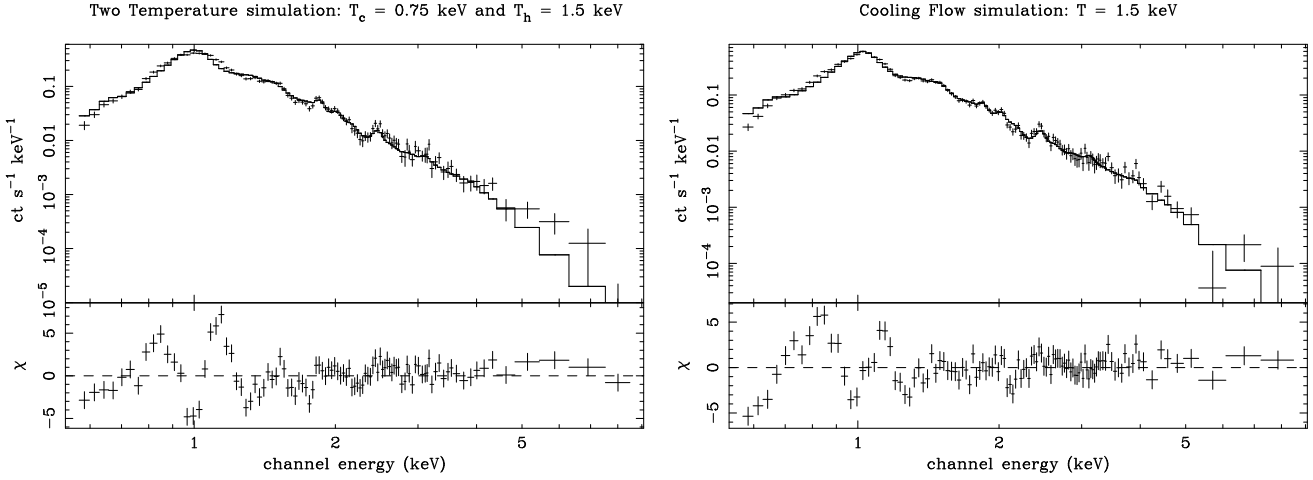
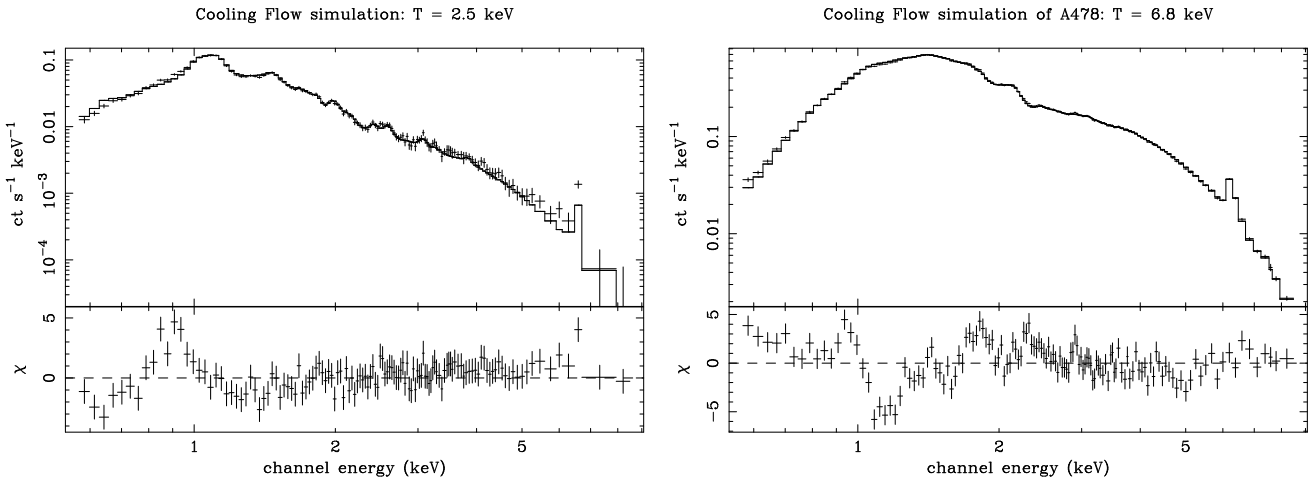
Model	Type	$N_{\text{H}}^{\text{c}}$ ( $10^{21} \text{ cm}^{-2}$ )	$N_{\text{H}}^{\text{h}}$ ( $10^{21} \text{ cm}^{-2}$ )	$T_{\text{c}}$ (keV)	$T_{\text{h}}$ (keV)	$Z$ ( $Z_{\odot}$ )	$\text{EM}_{\text{c}}$ or $\dot{M}$ (see notes)	$\text{EM}_{\text{h}}$ (see notes)
1	2T	2.5	0.5	0.75	1.5	1.0	2.0	2.0
2	CF+1T	2.5	0.5	1.5	tied	1.0	1.5	2.0
3	CF+1T	2.5	0.5	2.5	tied	1.0	10.0	1.5
4	CF+1T	6.8	2.2	6.8	tied	0.34	653	22.4

The units of emission measure (EM) are defined as in the notes to Table 4, and the mass deposition rates ( $\dot{M}$ ) are listed in units of  $M_{\odot} \text{ yr}^{-1}$ . See text for further explanation of these models.

**Table A2.** 1T fits to simulated data

Model	$N_{\text{H}}$ ( $10^{21} \text{ cm}^{-2}$ )	$T$ (keV)	$Z_{\text{Fe}}$ ( $Z_{\odot}$ )	$Z_{\text{O}}$ ( $Z_{\odot}$ )	$Z_{\text{Ne}}$ ( $Z_{\odot}$ )	$Z_{\text{Mg}}$ ( $Z_{\odot}$ )	$Z_{\text{Si}}$ ( $Z_{\odot}$ )	$Z_{\text{S}}$ ( $Z_{\odot}$ )
1	0.74	1.03	0.26	0.00	0.00	0.15	0.30	0.42
2	0.35	1.16	0.31	0.00	0.00	0.27	0.32	0.45
3	0.30	2.20	0.66	0.00	1.39	0.67	0.71	0.79
4	3.47	5.00	0.33	2.34	0.94	0.44	0.64	0.55

Best-fitting 1T model parameters resulting from fits to simulated ASCA data of the models in Table A1. All elements not listed have abundances tied to Fe in their solar ratios. See text for discussion of the ASCA simulations.

**Figure A1.** Best-fitting 1T models and residuals for the simulated ASCA data of models 1 (left) and 2 (right) listed in Table A1. These 1T fits have the  $\alpha/\text{Fe}$  ratios fixed at the solar values to highlight the residuals near the regions of the strong emission lines of the  $\alpha$ -process elements.**Figure A2.** As Figure A1 except we display results for the simulated ASCA data of models 3 (left) and 4 (right) of Table A1.

A physical explanation of the Fe bias is as follows. For models 1 and 2 which have average temperatures  $\sim 1$  keV, the colder temperature components preferentially excite emission lines in the Fe L complex below 1 keV (from ions Fe xvii - xxi) while the hotter temperature components preferentially excite the Fe L lines from  $\sim 1$ -1.4 keV (Fe xxi - xxiv). Since these components contribute approximately equally to the emission measure, the net result is that the spectral shape in the highly temperature-sensitive Fe L energy region is flattened with respect to a 1T model. That is, the spectrum of a 1T model which has the average temperature of the two components of models 1 or 2 (and has the same Fe abundance) will preferentially excite the Fe L lines right at 1 keV at the expense of the other Fe L lines near  $\sim 0.7$  keV and  $\sim 1.3$  keV and thus will be more peaked at 1 keV than either model 1 or 2. To partially compensate for this, i.e. to flatten the spectral shape near 1 keV, the 1T model decreases its Fe abundance so that the contribution of the flatter bremsstrahlung continuum is increased in the model. However, the distinctive residual pattern in Figure A1 demonstrates that the Fe L lines are sufficiently temperature sensitive (and the SIS has sufficient energy resolution) to thwart this attempt to successfully fit the 1T model to the simulated two-temperature and cooling flow spectra.

The strong temperature-sensitive Fe L emission lines are the key to this Fe bias. As one moves to higher temperatures (models 3 and 4) the Fe L lines become weaker and the bias decreases rapidly for average temperatures above 2 keV. Moreover, at higher temperatures the strong 6.5 keV Fe K emission line complex becomes increasingly more important and dominates the determination of the Fe abundance.

A final note: since it is the variation of the spectral shape of the Fe L complex with temperature which gives rise to the Fe bias, one does not obtain a biased measurement of the Fe abundance using a 1T model if the spectrum consists of multiple spectral components which have the same temperature but different Fe abundances. In this case the 1T model yields a value for the Fe abundance that is a weighted average over the various components.

## A2 The Si and S bias

Prominent residuals in the 1T fits ( $\alpha/\text{Fe}$  fixed at solar) are located near the strong emission lines of O, Ne, Mg, Si, and S (Figures A1 and A2). If the abundances of these elements are allowed to vary separately from Fe we obtain the results listed in Table A2. Although in most instances the O, Ne, and (to a lesser extent) the Mg abundances differ significantly from Fe, their new values do not correspond to a substantial reduction of the residuals over  $\sim 0.5$ -1.5 keV.

The 1T fits for models 1 and 2 produce zero O and Ne abundances and Mg/Fe ratios less than solar. These results are very sensitive to the presence of excess absorption on the colder temperature component. If instead we consider a model identical to model 1 but with  $N_{\text{H}}^{\text{c}} = N_{\text{H}}^{\text{h}} = 5 \times 10^{20} \text{ cm}^{-2}$ , then we obtain  $Z_{\text{O}} = 0.55Z_{\odot}$ ,  $Z_{\text{Ne}} = 1.1Z_{\odot}$ , and  $Z_{\text{Mg}} = 0.23Z_{\odot}$  with  $Z_{\text{Fe}} = 0.26Z_{\odot}$ .

For models 3 and 4 the 1T fits yield O, Ne, and Mg abundances very different from models 1 and 2 and from each other. Although the 1T fit for model 3 gives zero O abundance its large Ne abundance is qualitatively different from models 1 and 2. The ratios of O/Fe, Ne/Fe, and

Mg/Fe obtained for model 4 are all very much in excess of solar. Hence, the O, Ne, and Mg abundances are very sensitive to the temperature model and to the absorption model, and thus the systematic errors introduced when using a 1T model to measure these abundances are more complex in origin than the Fe bias discussed above.

In contrast, the  $\text{K}\alpha$  emission lines of Si and S are at sufficiently high energies so that they are not affected by the absorption model. The residuals near the Si ( $\sim 1.8$ -2.0 keV) and S ( $\sim 2.4$ -2.7 keV) lines are readily apparent for all the models in Figures A1 and A2, especially for model 4. The 1T fits with variable  $\alpha/\text{Fe}$  ratios listed in Table A2 for models 1-3 indicate modest ratios of  $\lesssim 1.1$  for  $Z_{\text{Si}}/Z_{\text{Fe}}$  and more substantial ratios of  $\sim 1.2$ -1.5 solar for  $Z_{\text{S}}/Z_{\text{Fe}}$ . Model 4 has the largest ratios with  $Z_{\text{Si}}/Z_{\text{Fe}} \sim 2$  and  $Z_{\text{S}}/Z_{\text{Fe}} \sim 1.7$ . Thus, the inferred values of Si/Fe tend to increase with temperature while the S/Fe ratio is relatively constant.

These excess Si/Fe and S/Fe ratios inferred by 1T models arise from two effects: (1) the colder temperature components present in the two-component models produce stronger Si and S emission, and (2) the 1T model underestimates the continuum at energies above  $\sim 2$  keV. Issue #1 is more important for the higher temperature systems like clusters (model 4) while issue #2 dominates for the lower temperature systems like elliptical galaxies (models 1-2).

Therefore, attempts to infer the Si/Fe and S/Fe ratios using isothermal models on spectra that are intrinsically composed of multiple temperature components will necessarily yield values for these ratios that are biased in excess of the true values, the effect of which is most important for higher temperature clusters of galaxies. This bias may have played a role in the excess Si/Fe ratios obtained by Mushotzky et al. (1996) and may in part explain the trend discovered by Fukazawa et al. (1998) that the Si/Fe ratio rises with temperature for clusters galaxies. Although Fukazawa et al. attempt to eliminate any problems associated with multiphase gas by excluding the central regions of their clusters, it is quite possible that their arbitrary method of defining the affected regions does not fully remove the effects of multiphase gas and the resulting Si bias we have described.

## REFERENCES

- Anders E., Grevesse N., 1989, *Geochimica et Cosmochimica Acta*, 53, 197  
Arimoto N., Matsushita K., Ishimaru Y., Ohashi T., Renzini A., 1997, *ApJ*, 477, 128  
Arnaud K., 1996, in Jacoby G. and Barnes J., eds., *Astronomical Data Analysis Software and Systems V*, ASP Conf. Series volume 101, p17  
Arnaud, M., Rothenflug, R., 1985, *A&AS*, 60, 425  
Arnaud, M., Raymond, J., 1992, *ApJ*, 398, 394  
Balucińska-Church M., McCammon D., 1992, 400, 699  
Beers T. C., Kriessler J. R., Bird C. M., Huchra J. P., 1995, *AJ*, 109, 874  
Bregman J. N., Hogg D. E., Roberts M. S., 1992, *ApJ*, 387, 484  
Brighenti F., Mathews W. G., 1998, *ApJ*, 495, 239  
Brighenti F., Mathews W. G., 1999a, *ApJ*, in press (astro-ph/9808175)  
Brighenti F., Mathews W. G., 1999b, *ApJ*, in press (astro-ph/9811258)  
Buote D. A., 1999, *MNRAS*, submitted (astro-ph/9811080) (B99)

- Buote D. A., Canizares C. R., 1994, *ApJ*, 427, 86
- Buote D. A., Fabian A. C., 1998, *MNRAS*, 296, 977 (BF)
- Buote D. A., Canizares C. R., Fabian A. C., Allen S. W., 1998, *MNRAS*, submitted (astro-ph/9804290)
- Canizares C. R., Fabbiano G., Trinchieri G., 1987, *ApJ*, 312, 503
- Ciotti L., D'Ercole A., Pellegrini S., Renzini A., 1991, *ApJ*, 376, 380
- Davis D. S., White III R. E., 1996, *ApJ*, 470, L35
- Davis D. S., Mushotzky R. F., Mulchaey J. S., Worrall D., Birkinshaw M., Burstein D., 1996, *ApJ*, 460, 601
- Davis D. S., Mulchaey J. S., Mushotzky R. F., 1999, *ApJ*, 511, 34
- de Vaucouleurs G., de Vaucouleurs A., Corwin H.G., Buta R. J., Paturel G., Fouqué P., 1991, *Third Reference Catalogue of Bright Galaxies* (Austin: Univ. Texas Press) (RC3)
- Dickey J. M., Lockman F. J., 1990, *ARA&A*, 28, 215
- Faber S. M., Wegner G., Burstein D., Davies R. L., Dressler A., Lynden-Bell D., Terlevich R. J., 1989, *ApJS*, 69, 763
- Fabian A. C., 1994, *ARA&A*, 32, 277
- Fabian A. C., Nulsen P. E. J., Canizares C. R., 1984, *Nature*, 310, 733
- Fabian A. C., Arnaud K. A., Bautz M. W., Tawara Y., 1994, *ApJ*, 436, L63
- Finoguenov A., Ponman T. J., 1999, *MNRAS*, in press (astro-ph/9901100)
- Finoguenov A., Jones C., Forman W., David L., 1999, *ApJ*, in press (astro-ph/9810107)
- Fujita Y., Fukumoto J., Okoshi K., 1997, *ApJ*, 488, 585
- Fukazawa Y., Ishida M., Ebisawa K., 1997, *Crab Calibrations on the XRT+GIS Energy Response Functions*, in *ASCA News* vol. 5, (NASA/GSFC: Greenbelt), 3
- Fukazawa Y., et al., 1998, *PASJ*, 50, 187
- Gendreau K., Yaqoob T., 1997, *ASCA XRT Calibration Issues*, in *ASCA News* vol. 5, (NASA/GSFC: Greenbelt), 8
- Hickson P., Mendes de Oliveira C., Huchra J. P., Palumbo G. G. C., 1992, *ApJ*, 399, 353
- Ikebe Y., et al., 1996, *Nature*, 379, 427
- Ikebe Y., et al., 1997, *ApJ*, 481, 660
- Ishimaru Y., Arimoto N., 1997, *PASJ*, 49, 1
- Johnstone R. M., Fabian A. C., Edge A. C., Thomas P. A., 1992, *MNRAS*, 255, 431
- Kunieda H., et al., *XRT Status Report*, in *ASCA News* vol. 5, (NASA/GSFC: Greenbelt), 3
- Liedahl D. A., Osterheld A. L., Goldstein W. H., 1995, *ApJ*, 438, L115
- Matsumoto H., Koyama K., Awaki H., Tsuru T., Loewenstein M., Matsushita K., 1997, *ApJ*, 482, 133
- Mewe R., Gronenschild E. H. B. M., van den Oord G. H. J., 1985, *A&AS*, 62, 197
- Mulchaey J. S., Zabludoff A. I., 1998, *ApJ*, 496, 73
- Mulchaey J. S., Zabludoff A. I., 1999, *ApJ*, in press (astro-ph/9810458)
- Mushotzky R. F., Loewenstein M., Arnaud K. A., Tamura T., Fukazawa Y., Matsushita K., Kikuchi K., Hatsukade I., 1996, *ApJ*, 466, 686
- Nulsen P. E. J., 1986, *MNRAS*, 221, 377
- Nulsen P. E. J., 1998, in Soker N. ed., *Galactic and Cluster Cooling Flows*, *ASP Conf. Series*, Vol. 115, (ASP: San Francisco), 135
- O'Dea C. P., Baum S. A., Maloney P. R., Tacconi L. J., Sparks W. B., 1994, *ApJ*, 422, 467
- Pellegrini S., Ciotti L., 1998, *A&A*, 333, 433
- Pildis R. A., Bregman J. N., Evrard A. E., 1995, *ApJ*, 443, 514
- Ponman T. J., Bourner P. D. J., Ebeling H., Böhringer H., 1996, *MNRAS*, 283, 690
- Ramella M., Geller M. J., Huchra J. P., Thorstensen J. R., 1995, *AJ*, 109, 1469
- Ramond J. C., Smith B. W., 1977, *ApJS*, 35, 419
- Renzini A., 1994, in Durret F., Mazure A., Tran Thanh Van J. eds., *Clusters of Galaxies*, (Gis-sur-Yvette: Editions Frontières), 221
- Renzini A., 1997, *ApJ*, 488, 35
- Renzini A., 1999, in Walsh J. and Rosa M., *Chemical Evolution from Zero to High Redshift*, (Berlin: Springer), in press (astro-ph/9902361)
- Renzini A., Ciotti L., D'Ercole A., Pellegrini S., 1993, *ApJ*, 419, 52
- Tanaka Y., Inoue H., & Holt S. S., 1994, *PASJ*, 46, L37
- Thomas P. A., Fabian A. C., Nulsen P. E. J., 1987, *MNRAS*, 228, 973
- Tonry J. L., Davis M., 1981, *ApJ*, 246, 666
- Trinchieri G., Fabbiano G., Kim D.-W., 1997, *A&A*, 318, 361
- Trinchieri G., Kim D.-W., Fabbiano G., Canizares C., 1994, *ApJ*, 428, 555
- Trümper J., 1983, *Adv. Space Res.*, 2, 241
- White D. A., Fabian A. C., 1995, *MNRAS*, 273, 72
- White R. E. III, Sarazin C. L., 1987, *ApJ*, 318, 621
- Xu H., Makishima K., Fukazawa Y., Ikebe Y., Kikuchi K., Ohashi T., Tamura T., 1998, *ApJ*, 500, 738
- Zabludoff A. I., Mulchaey J. S., 1998, *ApJ*, 496, 39